

CFL3D, FUN3D, and NSU3D Contributions to the Fifth Drag Prediction Workshop

Michael A. Park*

NASA Langley Research Center, Hampton, Virginia 23681

Kelly R. Laflin[†] and Mark S. Chaffin[‡]

Cessna Aircraft Company, Wichita, Kansas 67218

Nicholas Powell[§]

Gulfstream Aerospace Corporation, Savannah, Georgia 31402

and

David W. Levy[¶]

Cessna Aircraft Company, Wichita, Kansas 67218

DOI: 10.2514/1.C032613

Results presented at the Fifth Drag Prediction Workshop using CFL3D, FUN3D, and NSU3D are described. These are calculations on the workshop-provided grids and drag-adapted grids. The NSU3D results have been updated to reflect an improvement to skin-friction calculation on skewed grids. FUN3D results generated after the workshop are included for custom participant-generated grids, as well as a grid from a previous workshop. Uniform grid refinement at the design condition shows a tight grouping in calculated drag, where the variation in the pressure component of drag is larger than the skin-friction component. At this design condition, a fine-grid drag value was predicted with a smaller drag adjoint adapted grid via tetrahedral adaption to a metric and mixed-element subdivision. The buffet study produced a larger variation than the design case, which is attributed to large differences in the predicted side-of-body separation extent. Various modeling and discretization approaches had a strong impact on predicted side-of-body separation. A summary of similar published studies is provided to place these observations in context. This large wing-root separation bubble was not observed in wind-tunnel tests, indicating that more work is necessary in modeling wing-root juncture flows to consistently predict experiments.

Nomenclature

α	=	angle of attack
AR	=	aspect ratio
BL _{BUB}	=	separation bubble butt line
CD _{PRDrag}	=	coefficient due to pressure
CD _{SFDrag}	=	coefficient due to skin friction
CD _{TOT}	=	total drag coefficient
CL	=	coefficient of lift
CL _{TOT}	=	total coefficient of lift
CM _{TOT}	=	total pitching moment coefficient
c _{ref}	=	mean aerodynamic chord
FS _{BUB}	=	separation bubble fuselage station
H	=	Mach Hessian
H2	=	characteristic grid length, squared
h	=	output-based spacing
I	=	adaptation intensity
M	=	grid metric
N	=	total number of control volumes
Q	=	flow solution
t	=	output-based error tolerance
y ⁺	=	dimensionless wall distance

κ	=	control volume
λ	=	adjoint solution
χ	=	U-MUSCL scheme coefficient

I. Introduction

THE AIAA Drag Prediction Workshop (DPW) series has been an invaluable forum to evaluate computational fluid dynamics (CFD) tools. A detailed history of the DPW series and its objective are available from the overview prepared by Levy et al. [1] and the statistical analysis of Morrison [2]. The workshop series history has also been examined in the context of verification and validation by Morrison et al. [3]. This paper is intended to document the contribution of three CFD tools to the Fifth DPW (DPW-V) with an emphasis on observations of side-of-body separation and its effect on computed forces and moments. A summary of key results from the Fourth DPW (DPW-IV) and DPW-V that both studied the Common Research Model (CRM) provide context for this DPW-V contribution.

II. Common Research Model

For DPW-IV, the Common Research Model was created. This wing-body configuration with optional horizontal tail and nacelle with pylons is designed to be representative of a contemporary high-performance transonic transport [4]. The CRM without nacelles was analyzed with and without a horizontal tail at DPW-IV [5,6]. The CRM without nacelles or horizontal tail was the focus of DPW-V. The derived reference quantities of the full-scale vehicle are summarized in Table 1, which correspond to the geometry and grids provided by the DPW committee. After DPW-IV, a wind-tunnel test was performed on this configuration at the NASA National Transonic Facility (NTF) [7]. Additional tests were performed at the NASA Ames Research Center's 11 ft wind tunnel [8] to quantify the repeatability of the measurements. The NTF data are denoted as NTF-RUN-44, and the NASA Ames Research Center's 11 ft data are denoted as 11FT-RUN-126 in Figs. 1 and 2. The NASA Ames

Presented as Paper 2013-0050 at the 51st Aerospace Sciences Meeting, Grapevine, TX, 7–10 January 2013; received 5 September 2013; revision received 27 February 2014; accepted for publication 28 February 2014; published online 13 June 2014. This material is declared a work of the U.S. Government and is not subject to copyright protection in the United States. Copies of this paper may be made for personal or internal use, on condition that the copier pay the \$10.00 per-copy fee to the Copyright Clearance Center, Inc., 222 Rosewood Drive, Danvers, MA 01923; include the code 1542-3868/14 and \$10.00 in correspondence with the CCC.

*Research Scientist, Computational AeroSciences Branch. Senior Member AIAA.

[†]Senior Specialist Engineer, AeroSciences. Associate Fellow AIAA.

[‡]Senior Specialist Engineer, AeroSciences. Senior Member AIAA.

[§]Engineer II, Applied Aerodynamics. Member AIAA.

[¶]Principal Engineer, AeroSciences. Associate Fellow AIAA.

Table 1 Reference geometry for the CRM

Parameter	Value
Mean aerodynamic chord c_{ref}	275.80 in.
Wing reference area/2	297,360 in. ²
Wingspan/2	1,159.75 in.
X moment center	1,325.9 in.
Z moment center	177.95 in.
Aspect ratio AR	9.0

Research Center's 11 ft wind-tunnel tests included pressure-sensitive paint [9] and skin-friction measurements [10]. The model support system is not included in the DPW-IV or DPW-V computational model. Including the support system causes a shift in lift, drag, and pitching moment, as noted in a computational investigation [11]. This was verified in an additional computational investigation [12], where adjusting the wing twist caused an additional shift in predicted forces and moment toward the wind-tunnel measurements. Hue [13] also showed that using the experimentally measured twist distribution reduced lift and improved the comparison with wind-tunnel measurements. Keye et al. [14] applied fluid-structure coupling and confirmed the shift in predicted forces and moment due to wing twist.

The DPW-IV summary by Vassberg et al. [5] shows a large increase in code-to-code variation in lift and pitching moment between 3 and 4 deg angles of attack for the CRM. This large increase in variation was attributed to a large range of predicted side-of-body separation size. This DPW-V study also indicates that differences in predicted side-of-body separation extent at angles of attack above the design condition dramatically increased the scatter of results. At DPW-IV, the participants were unsure of the validity of this side-of-body separation because the configuration was not wind-tunnel tested before DPW-IV. The wind-tunnel tests [7,8] after DPW-IV did not indicate the abrupt drop in lift associated with the side-of-body separation predicted by some of the DPW-IV participants. Neither the measured skin friction nor the oilflow visualizations [10] indicated a large wing-root separation bubble at a 4 deg angle of attack. Pressure-sensitive paint measurements [9] indicated the pressure distributions predicted by the computational methods without a massive separation bubble. While significant separation was not observed in the wind-tunnel test, it is likely that it is a valid solution to the discrete equations because it was reported by many of the participants of DPW-IV and DPW-V using a wide range of methods. This paper focuses on the question "Under what conditions and computational models are these solutions produced?" The question of whether these computational models represent the behaviors observed in the wind-tunnel tests is addressed in the DPW-V summary [1], but the summary does not identify the connection between the scheme and the wing-root separation bubble.

III. DPW-IV

DPW-IV [5] included a horizontal tail for most cases, except one tail-off case for the downwash study. Sclafani et al. [15] showed that the presence of the tail or varying the tail incidence has a smaller influence on side-of-body separation than other factors. This makes the observation of side-of-body separation for a tail-on configuration relevant for the tail-off case in DPW-V. The DPW-IV participants and others published evidence of a large range of predicted side-of-body separation sizes. Sclafani et al. [15] exercised CFL3D and a number of OVERFLOW discretization options on different grid topologies. A bubble was shown at a 4 deg angle of attack for CFL3D and OVERFLOW with an upwind scheme but not OVERFLOW with a central scheme. Modeling the full Navier-Stokes (FNS) viscous terms had a larger bubble than a thin-layer Navier-Stokes (TLNS) approximation for a number of different grids at a 4 deg angle of attack with OVERFLOW. Increasing the wing-root juncture grid resolution with a finer grid having lines orthogonal to the wing and fuselage surfaces increased the extent of separation. Mani et al. [16] used OVERFLOW to show a small bubble at the CRM design condition that shrunk with grid refinement. The bubble was larger with FNS than the TLNS approximation, consistent with Sclafani et al. [15], and BCFD simulations on a grid with more wing-root juncture refinement showed a larger bubble with TLNS that also shrank with grid refinement [16].

Yamamoto et al. [17] provided a detailed examination of the separation bubble at a tail incidence of 0 deg. They showed a large increase in separation from 3 to 4 deg angle of attack for the UPACS structured and TAS unstructured codes. Increasing the chordwise and

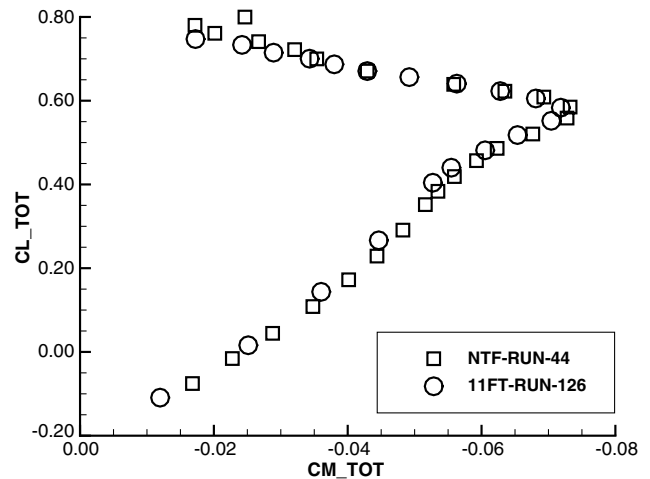
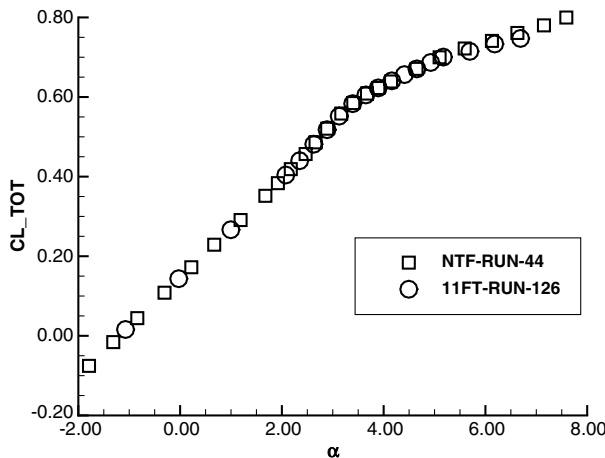
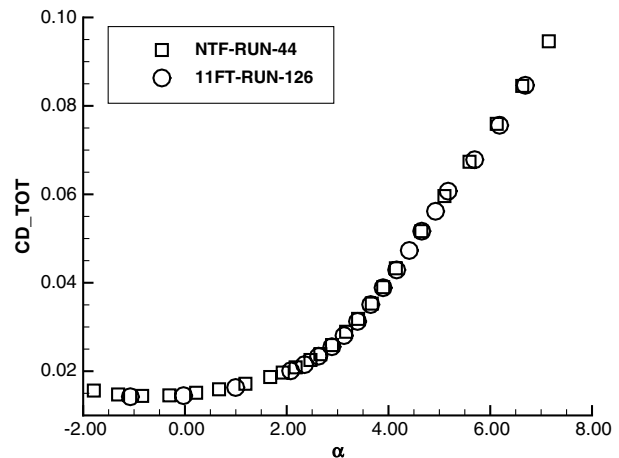


Fig. 2 Measured CRM wing-body lift coefficient as a function of pitching moment coefficient without nacelles or horizontal tail.



a) Coefficient of lift as a function of angle of attack



b) Coefficient of drag as a function of angle of attack

Fig. 1 Measured CRM wing-body forces without nacelles or horizontal tail.

spanwise grid resolution parametrically in the wing-root juncture region increased the extent of separation. Using the Quadratic Constitutive Relation (QCR) [18] nonlinear eddy-viscosity Reynolds stress term eliminated the bubble that was present with a linear eddy-viscosity Reynolds stress term. In a second paper, Yamamoto et al. [19] examined the CRM with and without QCR and found that QCR eliminated the bubble at a 4 deg angle of attack for both the shear-stress transport (SST) and Spalart–Allmaras (S–A) [20] turbulence models. Hashimoto et al. [21] applied three different grid topologies at a 4 deg angle of attack and concluded “The separation lines and C_p distribution are largely affected by grid topologies.” Refining the region between the wing and tail did not induce a significant change on wing-root juncture separation, as reported by Hashimoto et al. [22].

Brodersen et al. [23] predicted more separation on a prismatic boundary-layer grid having a refined wing-root juncture region than a hexahedral boundary-layer grid with a coarser wing-root juncture. Crippa [24] shows both attached and separated wing-root juncture flow. The SOLAR grid has a very coarse wing-root juncture grid due to a reduction of the boundary-layer hexahedra height in corners, which is a result of the SOLAR generation technique. A grid designated SolarChimera5 has an extremely well-refined wing-root juncture grid with an orthogonal overset C topology. The SolarChimera5 grid showed wing-root separation, but the original SOLAR grid did not show any separation in this region. The SolarChimera5 separation bubble was small at the design condition but grew dramatically in size at a 4 deg angle of attack for the S–A turbulence model. The S–A, S–A with rotation/curvature correction, and Reynolds stress turbulence models all had the same behavior at the design condition. Crippa also computed a local error estimate of dissipation on drag coefficient at the design condition, which indicated that dissipation in the coarse wing-root grid of the SOLAR grid had a significant impact on drag.

Lee-Rausch et al. [25] used a fine mixed-element wing-root juncture grid and FUN3D with the Venkatakrishnan limiter. A small wing-root separation bubble was shown at the design condition that grew larger with grid refinement. Mavriplis and Long [26] used the same mixed-element grids with NSU3D. They showed a small separation bubble in the wing-root juncture region and flow separation behind the primary upper wing shock at a 4 deg angle of attack. NSU3D uses an edge-based viscous operator, which results in a TLNS approximation on orthogonal grids. The Edge solver [27,28] was applied to various grid resolutions in the wing-root juncture and different turbulence models, but no separation was observed. Edge also uses an edge-based viscous operator.

Vos et al. [29] used six different structured multiblock grid systems to compare near-field and far-field drag methods. They indicated that separation was predicted with some of the grids, but details of the separation region extent were not provided. They indicated “Grid resolution is an important parameter which influences the resolution of these flow separations...” Other researchers [30–32] also examined the DPW-IV CRM cases, but they did not provide details of the wing-root juncture flow.

IV. DPW-V

The CRM wing-body configuration was examined in the subsequent workshop, DPW-V. DPW-IV identified that “Generating a consistent set of grids for the purpose of grid-convergence studies remains a challenge, especially for unstructured meshes [5].” In DPW-V, a common grid system with consistent grid refinement factors was required for all participants [33]. The base of the common grid system is a point-matched structured grid, which was converted for use with overset and unstructured grid flow solvers. This allows a large majority of methods used in previous workshops to be applied to consistently refined grids with identical point distributions. The variation of computed lift and pitching moment between flow solvers grew dramatically between 3 and 4 deg angles of attack for DPW-IV [5]. To better characterize this flow regime, the angle-of-attack resolution is increased to a quarter of a degree between 2.5 and 4 deg angles of attack for DPW-V. In support of the Turbulence Model

Table 2 Committee-supplied structured and hybrid grids

Grid level	Nodes	Hexahedra	Prisms	Tetrahedra
L1	660,177	638,976	425,984	2,555,904
L2	2,204,089	2,156,544	1,437,696	8,626,176
L3	5,196,193	5,111,808	3,301,376	20,766,720
L4	17,441,905	17,252,352	11,261,952	69,728,256
L5	41,231,169	40,894,464	26,411,008	166,133,760

Benchmarking Working Group, optional test cases from the Turbulence Modeling Resource Web site** were requested. The cases requested for DPW-V are listed here:

1) Case 1 is the Common Grid Study. The 0.5 lift coefficient CRM design condition is simulated on a series of DPW committee-provided uniformly refined grids to examine grid convergence.

2) Case 2 is the Buffet Study. Cases are requested on the medium DPW committee-provided grid at every quarter of a degree between 2.5 and 4 deg angles of attack where separation was observed in DPW-IV.

3) Case 3 (optional) is the Turbulence Model Verification. Three optional cases are specified to study the implementation of turbulence models in a controlled study.

A series of point-matched structured-block grids are provided by the DPW-V committee [33]. The committee converted the structured grids into an unstructured hexahedral grid format and formed hybrid grids by dividing these hexahedral elements into prisms and tetrahedra. The number of elements in the L1 to L5 grids is shown in Table 2. The L6 grid was not provided by the committee in hybrid form.

The DPW-IV side-of-body separation flow pattern was seen for some of the DPW-V buffet case solutions. Again, the presence of the side-of-body separation could not be isolated to a single factor. It appears to be a complex interaction of grid topology, grid resolution, numerical scheme, modeling of TLNS, and the application of QCR. Neither a break in lift or large side-of-body separation was observed in the wind-tunnel test, so Levy et al. [1] proposed the following:

The outliers were defined as solutions that exhibited a break in lift before $\alpha = 4$ deg (relative to the linear lift vs α slope), or exhibited lift and/or drag considerably outside the norm of the other solutions. Outliers were seen in solutions from all grid families, and from SA, SST, and Goldberg RT turbulence models [1]. Lift break, which is indicative of a large increase in flow separation, occurred as early as 3 deg angle-of-attack in five solutions. Seven solutions exhibited a lift break between 3.25 and 3.5 deg and a further nine solutions at a 3.75 deg angle-of-attack.”

These outliers are a significant portion of the over 50 DPW-V buffet submissions.

Scalafani et al. [34] described the OVERFLOW and BCFD contributions to DPW-V. OVERFLOW with QCR eliminated the large bubble at a 4 deg angle of attack on a medium DPW-IV grid with no tail that was present for the standard S–A. This finer DPW-IV grid with an orthogonal collar wing-root grid produced a bubble that was not observed on the DPW-V L2 grid. BCFD on a DPW-IV no-tail grid or the DPW-V common hexahedral grid did not show an abrupt drop in lift for the buffet case with the standard S–A. This implies that the TLNS BCFD solutions did not experience a large growth in bubble extent.

Hysteresis at the buffet angles of attack was reported on the L3, L2, and L1 hybrid grids by Nishikawa et al. [35] with FUN3D. Murayama et al. [36] also mapped a hysteresis loop with the UPACS flow solver on the L3 multiblock grid with the S–A and SST turbulence models. Murayama et al. showed a large separation bubble on the L3 common multiblock grid with standard S–A that was eliminated with QCR. A custom multiblock grid with grid lines orthogonal to wing and fuselage exhibited a bubble that grew with

**Data available online at <http://turbmodels.larc.nasa.gov> [retrieved 7 February 2012].

grid refinement. A custom Cartesian-dominated hexahedral grid showed attached flow. Gariepy et al. [37] applied ANSYS-Fluent 13.0 to the L3 and custom grid family developed by the IDEA Research Chair at Polytechnique Montréal with a refined wing-root junction. For both the S-A and κ - ω SST models, the medium IDEA grid showed a significant drop in lift and growth in bubble size during the buffet study, but the L3 grid did not. A coarse IDEA grid showed a milder drop in lift.

Keye et al. [14] observed a larger separation region on the L4 grid than the L3 grid with the DLR-TAU flow solver. S-A with QCR, SST, and an RST model produced less separation than S-A. A custom Centaur™ grid with a hexahedral wake block produced the largest separated region. Including fluid-structure coupling shifted the lift, drag, and pitching moment toward the wind-tunnel data but had a smaller effect on the overprediction of side-of-body separation than the grid and turbulence modeling. Illi et al. [38] also showed separation and inboard lift loss for S-A DLR-TAU on a custom grid with orthogonal grid lines to the fuselage and wing above a 3.2 deg angle of attack. Osusky et al. [39] showed separated streamlines and lift loss for S-A with the DIABLO flow solver on the L3 grid above a 3.2 deg angle of attack. Application of QCR to the S-A model eliminated the separation. Other researchers [13,40,41] contributed to DPW-V, but they did not provide details of the wing-root juncture flow of the buffet case.

This large body of work performed in conjunction with the DPW-IV and DPW-V indicates that the CRM side-of-body separation is very sensitive to the CFD scheme used, the grid topology, and the grid resolution. This sensitivity is especially high in the wing-root region. This side-of-body flow separation on the CRM appears to be the combination of both modeling and discretization issues. It is difficult to isolate all of the individual factors that result in the prediction of separated flow, but some trends appear evident from this review of past studies. The modeling options of TLNS and QCR appear to reduce the size of the separation bubble as compared to FNS with a linear eddy-viscosity Reynolds stress term, especially for the S-A model. The use of coarser grids or more dissipative convective schemes reduces the separation bubble extent or eliminates this separation completely.

V. Method Description

Three Reynolds-averaged Navier-Stokes (RANS) codes are used in this study. CFL3D, FUN3D, and NSU3D have applicability to a large range of configurations and provide a large range of options. Only the options used on the CRM in this study are described. For the constant coefficient of lift CL grid convergence study, all three codes employ a CL driver that allows convergence to a fixed lift coefficient value. Based on user-defined inputs, the codes periodically adjust the angle of attack during the computation based on the current CL value until the prescribed CL value is achieved at convergence.

A. CFL3D Flow Solver

CFL3D [42] is a structured-grid multizone cell-centered finite volume method. It was applied to previous workshops, including DPW-IV [15]. It uses an upwind-biased spatial differencing on the convective and pressure terms, and second-order differencing on the viscous terms. Roe's flux difference-splitting method [43] is used to obtain fluxes at the cell faces. The option in CFL3D to model the FNS mean-flow equations is exercised for all cases. Only the S-A one-equation turbulence model was used for this study. The turbulence model diffusion terms use the thin-layer approximation. The mean-flow equations are advanced in time with the eddy viscosity fixed, and then the turbulence model is advanced in time with the mean-flow solution fixed. This alternating turbulence model and mean-flow iteration technique is named the loosely coupled iteration. The solution is advanced in time with an implicit approximate factorization method. CFL3D employs local time-step scaling, grid sequencing, and a multigrid to accelerate convergence to steady state.

B. FUN3D Flow Solver

FUN3D [44,45] is a finite volume RANS solver in which the flow variables are stored at the vertices or nodes of the mesh. FUN3D was

used in previous workshops, including DPW-IV [25]. FUN3D solves the equations on mixed-element grids, including tetrahedra, pyramids, prisms, and hexahedra. At interfaces delimiting neighboring control volumes, the inviscid fluxes are computed using an approximate Riemann solver based on the values on either side of the interface. Roe's flux difference splitting [43] is used in the current study. For second-order accuracy, interface values are obtained by a U-MUSCL scheme [46,47], with gradients computed at the mesh vertices using an unweighted least-squares technique. The U-MUSCL scheme coefficient χ is set to 0.0 for purely tetrahedral grids and to 0.5 for grids with mixed-element types. The Venkatakrishnan limiter [48] is used for some cases in this study. This dimensional limiter is scaled to the mean aerodynamic chord to have the same behavior as the airfoil example with unit chord by Venkatakrishnan [48].

For tetrahedral meshes, the full viscous fluxes are discretized using a finite volume formulation in which the required velocity gradients on the dual faces are computed using the Green-Gauss theorem. On tetrahedral meshes, this is equivalent to a Galerkin-type approximation. For non-tetrahedral meshes, the same Green-Gauss approach can lead to odd-even decoupling. A pure edge-based approach can be used to circumvent the odd-even decoupling issue but yields only approximate viscous terms. For non-tetrahedral meshes, the edge-based gradients are combined with Green-Gauss gradients; this improves the h ellipticity of the operator and allows the complete viscous stresses to be evaluated [44,49]. This formulation results in a discretization of the FNS equations. The option of only using edge-based viscous terms (equivalent to a TLNS approximation for orthogonal grids) is also available and is used for a dataset in this study. The diffusion term in the turbulence model is handled in the same fashion as the mean-flow viscous operator.

The S-A model may be solved loosely coupled to the mean-flow equations in the same fashion as CFL3D. FUN3D also provides a tightly coupled iteration where the turbulence model and mean-flow equations are updated simultaneously with a linearization of all coupling terms. The cases for DPW-V were computed assuming fully turbulent flow. The negative S-A model [50] is available as well as the original model. The negative S-A model exhibits better iterative convergence properties, especially in the highly clustered wake region of the DPW-V committee-provided grids.

The solution at each time step is updated with a backward Euler time-differencing scheme. At each time step, the linear system of equations is approximately solved with either a multicolor point-implicit procedure or an implicit-line relaxation scheme. This implicit relaxation scheme can be used as a preconditioner to a generalized conjugate residual (GCR) [51] for stabilization and convergence acceleration. Local time-step scaling is employed to accelerate convergence to steady state. Two other options are exercised on some cases to improve iterative convergence rate and robustness: a Jacobian-free Newton method, and an adaptive CFL specification. The Newton method used full linearization of the nonlinear residual with a pseudotime addition. It is computed with a first-order Fréchet derivative to enhance the standard defect correction approach [35]. The solution of this exact linearization is also wrapped with the GCR for stabilization and convergence acceleration. The CFL specification for the nonlinear pseudotime term and the preconditioner can be adjusted with an adaptive approach [35].

C. NSU3D Flow Solver

The NSU3D code is an unstructured mesh multigrid RANS solver for high-Reynolds-number external aerodynamic applications. It has been used in previous workshops, including DPW-IV [26]. The NSU3D discretization employs a vertex-based approach where the unknown fluid and turbulence variables are stored at the vertices of the mesh. The fluxes are computed on faces delimiting dual-control volumes, with each dual face being associated with a mesh edge. This discretization operates on hybrid mixed-element meshes. Generally, prismatic elements are employed in highly stretched boundary-layer regions and tetrahedral elements are employed in isotropic regions of the mesh away from the aircraft surfaces.

The convective terms are discretized as central differences with added matrix dissipation. Second-order accuracy is achieved by formulating these dissipative terms as an undivided biharmonic operator, which is constructed in two passes of a nearest-neighbor Laplacian operator. In the matrix form, this dissipation is similar to that produced by a Riemann solver gradient-based reconstruction scheme. It is obtained by replacing the difference in the reconstructed states on each side of the control volume interface by the undivided differences along mesh edges resulting from the biharmonic operator construction. These differences are then multiplied by the characteristic matrix to obtain the final dissipation terms.

The baseline NSU3D discretization employs a finite difference scheme to approximate the thin-layer form of the viscous terms for the Navier–Stokes (N–S) equations, although this is done in a multidimensional fashion, by computing a Laplacian of the velocity field [52]. The main approximation in this approach is the omission of the cross-derivative viscous terms and the assumption of a locally constant viscosity. NSU3D incorporates the S–A turbulence model, and the cases for DPW-V were run fully turbulent.

The basic time-stepping scheme in NSU3D consists of a three-stage explicit scheme. Convergence is accelerated by a local block-Jacobi preconditioner in regions of isotropic grid cells. In boundary-layer regions, where the grid is highly stretched, a line preconditioner is employed to relieve the stiffness associated with the mesh anisotropy [53]. An agglomeration multigrid algorithm is used to further enhance convergence to steady state [52,54]. The multigrid solver is implemented as a nonlinear full approximation scheme solver. The Jacobi and line preconditioners are used to drive the various levels of the multigrid sequence.

At DPW-V, it was noted that NSU3D predicted lower skin-friction values than the other methods presented. This observation led to an examination of the skin-friction calculation method in NSU3D. The grid lines in the DPW-V committee-provided grids were determined to be less orthogonal to the solid surfaces than typically experienced. To improve the NSU3D DPW-V results, a more general skin-friction calculation was implemented in NSU3D that accommodates non-orthogonal grid line intersections with viscous surfaces.

In the original implementation, the normal velocity gradient required in the skin-friction calculation was computed by dividing the difference in the velocity at the first point off the wall and the velocity at the wall (which is zero) by the distance between these two points. This formulation is inaccurate for grid lines that are not normal to the wall surface. Therefore, two revised approaches have been implemented and compared. In the first approach, the distance used to compute the velocity gradient is replaced by the normal distance to the wall for the off-body grid point as computed for the turbulence model routine. In the second approach, the tangential components of shear stress are computed using a Green–Gauss integration to obtain the required velocity gradients within the wall-bounded mesh cells. Both approaches were found to agree very closely with each other and yielded higher skin-friction values on the

committee-provided grids, although insignificant differences were observed between the new approaches and the original approach on previous DPW workshop grids generated using the VGRID [55] advancing layer mesher. The general skin-friction calculation method that accounts for grid lines that are not normal to the wall surface is used in this study.

VI. Test Cases and Results

The required test cases for DPW-V are a uniform grid convergence study at constant lift with committee-provided grids and a buffet study on the medium L3 grid between 2.5 and 4 deg angles of attack. For all cases, the Mach number is 0.85 and the Reynolds number is 5 million, based on the mean aerodynamic chord. The uniform refinement study is performed for CFL3D, NSU3D, and FUN3D with and without the Venkatakrishnan limiter. The uniform refinement results provide an excellent verification dataset for the FUN3D output-adaptive scheme applied to the L1 hybrid grid at the design conditions. This allows the adaptive scheme to be compared to a consistently refined set of grids. The buffet study is partitioned into applying different CFD schemes to DPW-V L3 medium grids and applying FUN3D to grids with different grid topologies. The optional turbulence model verification test cases where not provided here, but CFL3D and FUN3D results are available for a majority of the Turbulence Modeling Resource Web site examples (see footnote **) and are included in the DPW-V summary [1].

A. Grid Convergence Study

A grid convergence study was performed at the design condition of 0.5 coefficient of lift. The L1–L6 structured grids were provided by the DPW committee, but CFL3D failed to reach satisfactory iterative convergence on the L6 grid. So, only the L1–L5 results are presented for CFL3D. NSU3D results are only available for the L1–L4 grids and use the improved skin-friction calculation for nonorthogonal grids. Only L1–L5 grids are analyzed with FUN3D, because the L6 grid was not provided by the committee in hybrid form.

Drag coefficient CD_{TOT} is plotted as a function of a characteristic length squared $H2$ in Fig. 3a, and pitching moment coefficient CM_{TOT} is plotted as a function of $H2$ in Fig. 3b. $H2$ is computed as $N^{-2/3}$, where N is the number of control volumes. This exponent is based on two assumptions: the characteristic length of the grid varies with the cube root of the cell volume, and the error in the solution decreases asymptotically with the characteristic length squared for a second-order method. When these assumptions are met, the computed outputs should vary linearly with $H2$. The legend description FUN3D is FNS without a limiter, and FUN3D-V is FNS with the Venkatakrishnan limiter. On the finer grids, the difference between FUN3D-V and FUN3D diminishes. The CD_{TOT} values of the finest-grid FUN3D, FUN3D-V, and CFL3D are within one count, 0.0001, of drag coefficient. The finest grid NSU3D simulation (L4)

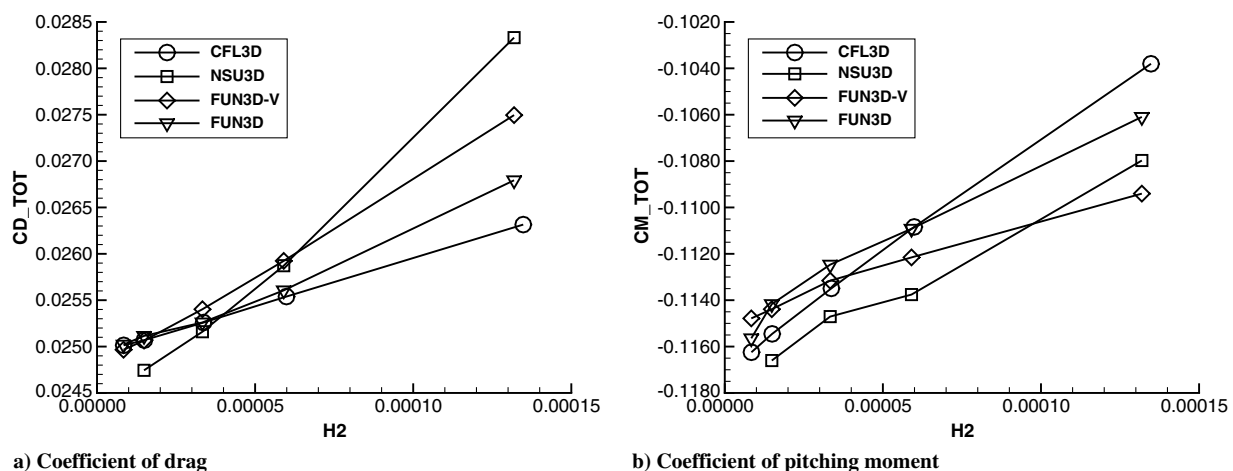


Fig. 3 Coefficient of drag and pitching moment as a function of characteristic grid spacing at $CL = 0.5$ for uniformly refined grids.

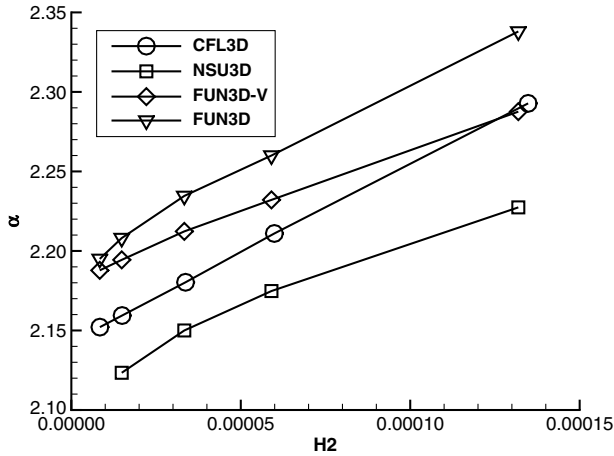


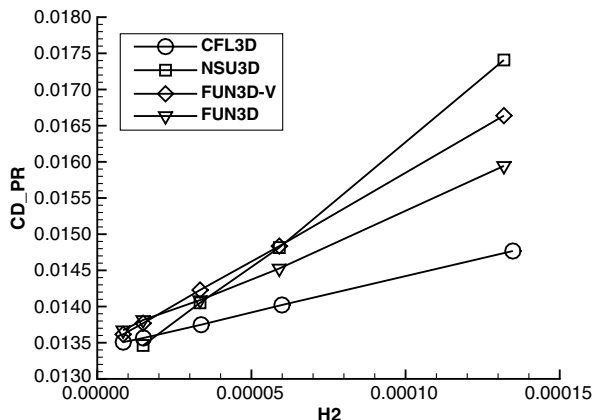
Fig. 4 Angle of attack as a function of characteristic grid spacing at $CL = 0.5$ for uniformly refined grids.

predicted a slightly lower CD_{TOT} than the L4 grid simulations of the other methods. All four methods indicated CM_{TOT} became more negative as the grid was refined. The angle of attack α required for a coefficient of lift of 0.5 is shown in Fig. 4. This α decreased consistently across the methods as the grid was refined. This decrease in α with grid refinement at constant coefficient of lift is analogous to an increase in coefficient of lift with grid refinement at constant α .

The pressure CD_{PR} and skin friction CD_{SF} components of CD_{TOT} are shown in Fig. 5. CD_{SF} exhibits a larger variation than CD_{TOT} . The CD_{PR} is very similar for FUN3D and FUN3D-V on the two finest grids, but the difference between the methods decrease with grid refinement. The CFL3D CD_{SF} is extremely insensitive to grid resolution. The three unstructured grid methods show a very similar trend of increasing CD_{SF} with grid refinement. The skin-friction calculation method is similar for CFL3D and the unstructured grid methods. The formation of the convection terms is the most significant difference between the cell-based structured CFL3D and the node-based unstructured methods. CFL3D and FUN3D are shown to converge to the same pressure and skin-friction drag values on the Turbulence Modeling Resource test cases with uniform grid refinement, but they have different drag values on coarser grids (see footnote **).

B. Output-Based Grid Adaptation

Output-based adaptation has been applied to the Shock-Boundary-Layer Interaction Workshop [56] and the High Lift Prediction Workshop [57]. These previous applications had significant off-body features that allowed the use of adaptive mechanics with a frozen boundary-layer region. Drag calculation on the CRM configuration is



a) Pressure contributions to coefficient of drag

very sensitive to surface and boundary-layer resolution, so a frozen boundary-layer approach is not suitable. A boundary element subdivision technique was implemented for this study to refine surface and boundary-layer grids in conjunction with the off-body tetrahedral regions.

An example of an adapted prismatic and tetrahedral flat-plate boundary-layer grid is shown in Fig. 6. Figure 6a shows the original grid, and Fig. 6b shows an example of an adapted grid to illustrate the method. The lower near-body portion of the grid is constructed of stacks of prismatic elements, and the upper portion outside of the boundary-layer prismatic grid contains tetrahedral elements. In Fig. 6b, the prismatic stacks have been subdivided tangentially to the lower surface.

The prism stacks are not refined in the normal direction in this application because the initial CRM grid met the $y^+ < 1$ turbulence model recommendation for a majority of the solid boundaries. A fixed fraction of prism element sides with the largest adaptive intensity are flagged for refinement. For this flat-plate illustration, the jump in density over the edge is the adaptive intensity. For the CRM, the scalar Venditti [58] remaining error estimate is modified by Park [59] to use reconstructed flow and adjoint solutions on the current grid:

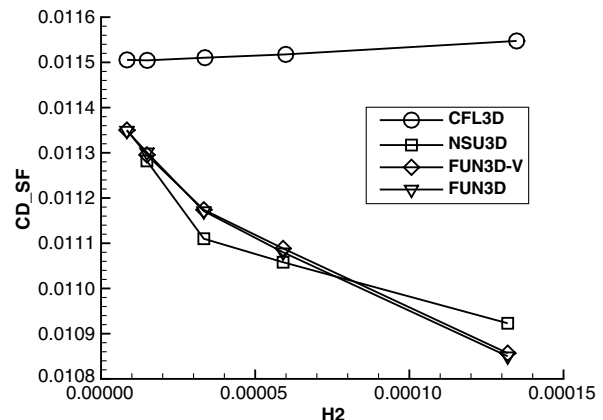
$$[I]_k = \frac{1}{2} \sum_{i=1}^6 \{ |R^\lambda(\hat{\lambda})|_{i,k} [\hat{Q} - \bar{Q}]_{i,k} + |[\hat{\lambda} - \bar{\lambda}]_{i,k} [R(\hat{Q})]_{i,k} \} \quad (1)$$

where \hat{Q} and $\hat{\lambda}$ have been reconstructed quadratically, \bar{Q} and $\bar{\lambda}$ have been reconstructed linearly, and i loops over the six governing equations (including the S-A model). The refinement flags are propagated up and down the sides of the prism stacks so that all prisms in a stack are refined the same manner. New nodes introduced on the boundary are placed on a linear, faceted representation of the surface; the new nodes are not projected to the actual geometry.

An anisotropic metric specifies the request for the adapted tetrahedra density and orientation. In the flat-plate illustration, the absolute value of the Mach Hessian $|H|$ scaled by density jumps of Bibb et al. [60] is the specified metric M . For the CRM, the Venditti [58] output-based metric is specified, where $|H|$ is scaled by the output-based spacing h :

$$h_k = h_k^0 \left(\frac{t^2}{NI_k \sum I_k} \right)^\omega \quad (2)$$

It includes a user-specified error tolerance t , the total number of control volumes N , an estimate of the current grid size h^0 , and an a priori estimate of error convergence rates [58]. Whereas the prism stacks are only enriched by subdivision, the tetrahedral grid is both refined and coarsened to comply with the metric. A parallel metric-based scheme with element splitting, element collapse, element



b) Skin-friction contributions to coefficient of drag

Fig. 5 Components of coefficient of drag as a function of characteristic grid spacing at $CL = 0.5$ for uniformly refined grids.

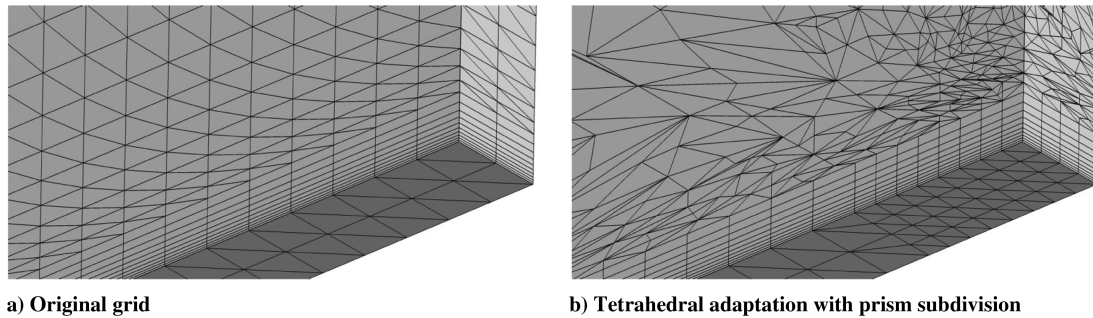


Fig. 6 Flat-plate grid illustrating adaptation technique.

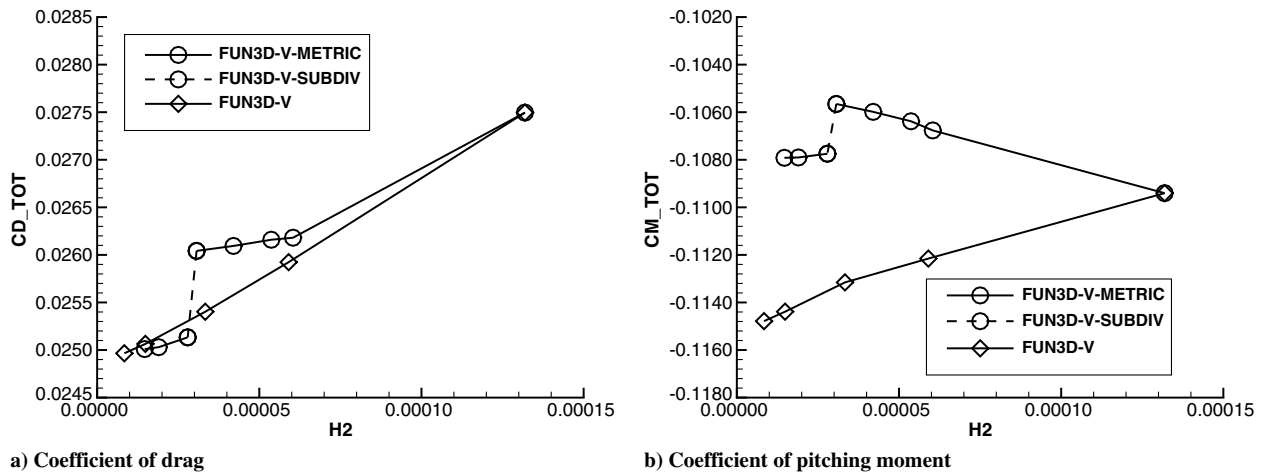


Fig. 7 Coefficient of drag and pitching moment as a function of characteristic grid spacing at $CL = 0.5$ for uniformly refined and adapted grids.

swap, and node movement [59,61] is used to modify the tetrahedral elements.

Figure 7a shows the effects of uniform refinement (FUN3D-V from Fig. 3a) and drag adaptation on CD_{TOT} . FUN3D-V-METRIC is the existing metric-based scheme with frozen prismatic elements. FUN3D-V-SUBDIV is the new edge primitive scheme that includes fixed fraction prismatic element subdivision. The first four FUN3D-V-METRIC adaptations (without FUN3D-V-SUBDIV) appear to predict a higher drag value than uniform refinement, which includes refinement in the boundary layer. The next adaptation includes subdivision of the boundary-layer prisms (FUN3D-V-SUBDIV) and produces a large reduction in drag. The three final FUN3D-V-METRIC adaptations appear to approach the uniformly refined grid CD_{TOT} but do so with a smaller grid. The pitching moment, CM_{TOT} in Fig. 7b, appears to be approaching a less negative value than the uniformly refined grids. The FUN3D-V-SUBDIV subdivision has a significant effect on the value of pitching moment and its trend with further metric-based adaptation. The angle of attack required to maintain $CL = 0.5$ is fraction of a degree higher for the adapted grid than the uniformly refined grids; see Fig. 8. The pressure and skin-friction components of drag are separated in Fig. 9. The pressure drag is at or higher than the uniformly refined grid values, and the skin-friction drag is lower.

Boundary-layer prism subdivision FUN3D-V-SUBDIV has a significant impact on forces and moment for this case. The choice of the number of FUN3D-V-METRIC and FUN3D-V-SUBDIV adaptations are arbitrary in this application. As in Ceze and Fidkowski, [40], the geometry is fixed during surface adaptation but on the linear L1 surface grid. Work is ongoing to generalize and better integrate the subdivision with the metric-based adaptation to retain the benefits of both methods in a more efficient and automated manner.

Lee and Pulliam [62] applied an overset adaptation scheme to the DPW-IV CRM configuration with horizontal tail, but their adaptation

scheme appears to asymptote to larger coefficient of drag values than uniformly refined grids. Element subdivision (triggered by the undivided gradient of density) has been used on a transport configuration by Mavriplis [63], but the effect on computed forces was not provided.

The original and adapted surface grids are shown in Fig. 10. A majority of the wing is refined with the nose, tail, and fuselage over the wing. The original and adapted symmetry planes are shown in Fig. 11; the artifacts of the structured grid generation are shown as a tightly packed grid emanating from the top and bottom of the nose and tail. These structured-grid artifacts are removed by the grid adaptation, and the wake behind the fuselage is refined.

High-density pockets of the grid are seen in Fig. 11b. They are examined by investigating the requested change in grid size h/h^0 in

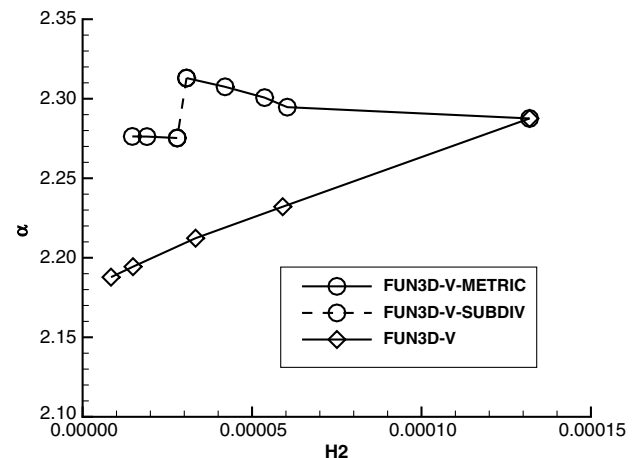


Fig. 8 Angle of attack as a function of characteristic grid spacing at $CL = 0.5$ for uniformly refined and adapted grids.

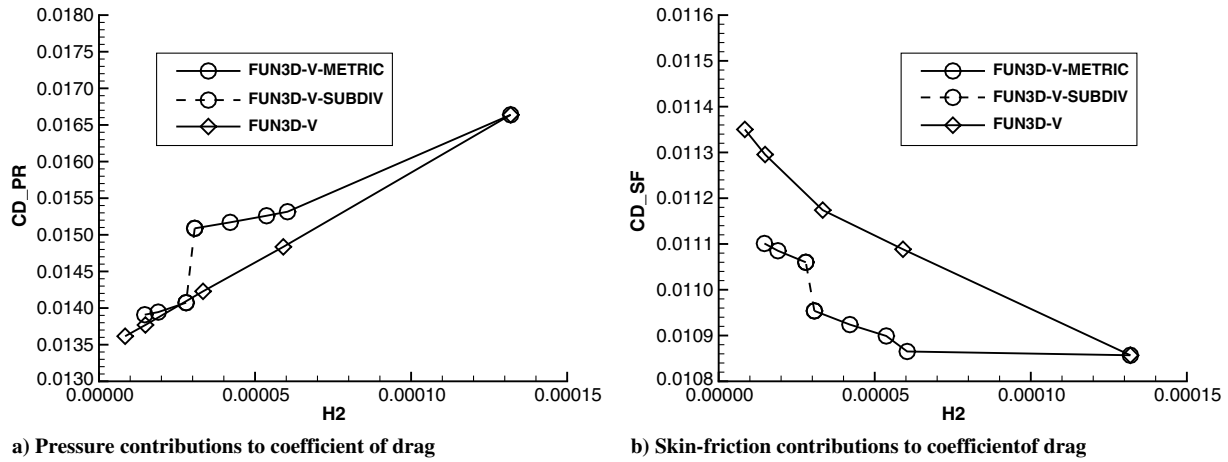


Fig. 9 Components of coefficient of drag as a function of characteristic grid spacing at $CL = 0.5$ for uniformly refined and adapted grids.

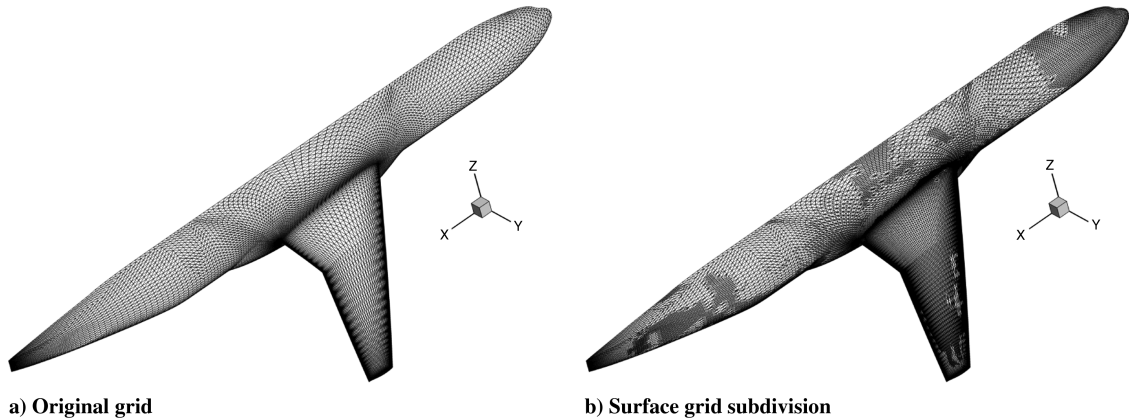


Fig. 10 CRM surface grid.

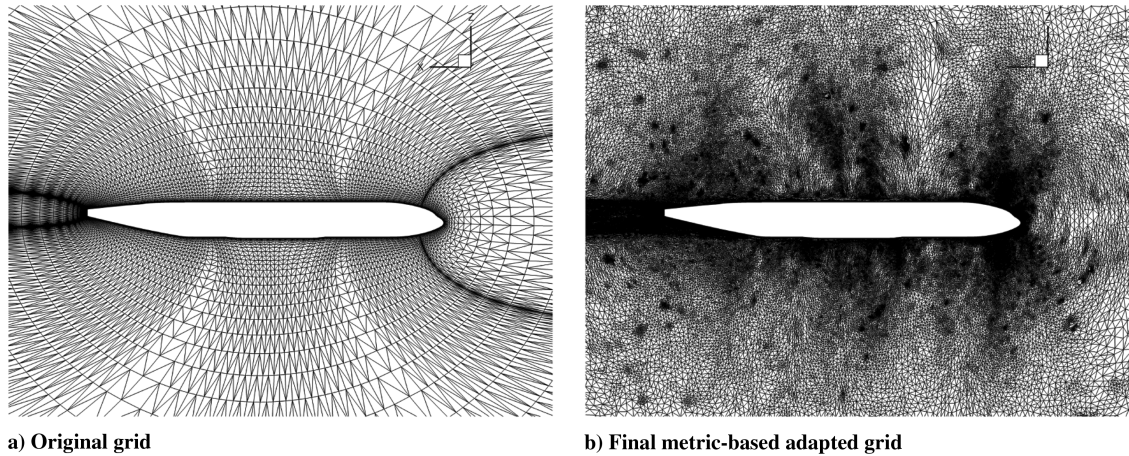


Fig. 11 CRM symmetry plane grids.

Fig. 12a and the current spacing estimate h^0 in Fig. 12b. Equation (2) provides the relation between h and h^0 . The current spacing is estimated by computing the largest eigenvalue of the implied tetrahedral metric [64]. The high-density pockets are seen in Fig. 12b as localized regions of lower h than the surrounding grid. The output-based grid scaling request is greater than unity in these areas, indicating that coarsening is requested. It appears that noise in the current spacing estimated is causing the grid to be refined in these high-density pockets and not the output-based scaling request. Mesh gradation control [65] may be a viable method to filter this noise, or a metric that does not require a current spacing estimate could be implemented [66]. Mach number and continuity equation adjoint are shown on the original L1 grid in Fig. 13. The grid is refined (Figs. 12

and 11b) in regions where the residuals weighted with an estimate of interpolation error are large [Eq. (1)].

C. Buffet Study (Committee-Provided Grids)

The lift CL_{TOT} and drag CD_{TOT} coefficients for the L3 DPW-V committee-provided grids are plotted as angle of attack α increases in 0.25 deg increments in Fig. 14. FUN3D-V denotes FNS with the Venkatakrishnan limiter, FUN3D denotes FNS with unlimited reconstruction, and FUN3D-TL denotes edge-based N-S terms with unlimited reconstruction. CFL3D, NSU3D, and FUN3D-TL show very similar trends. FUN3D and FUN3D-V both show dramatic reductions in CL_{TOT} and CD_{TOT} , but the limiter delays and reduces the magnitude of the reduction. CL_{TOT} is plotted as a function of

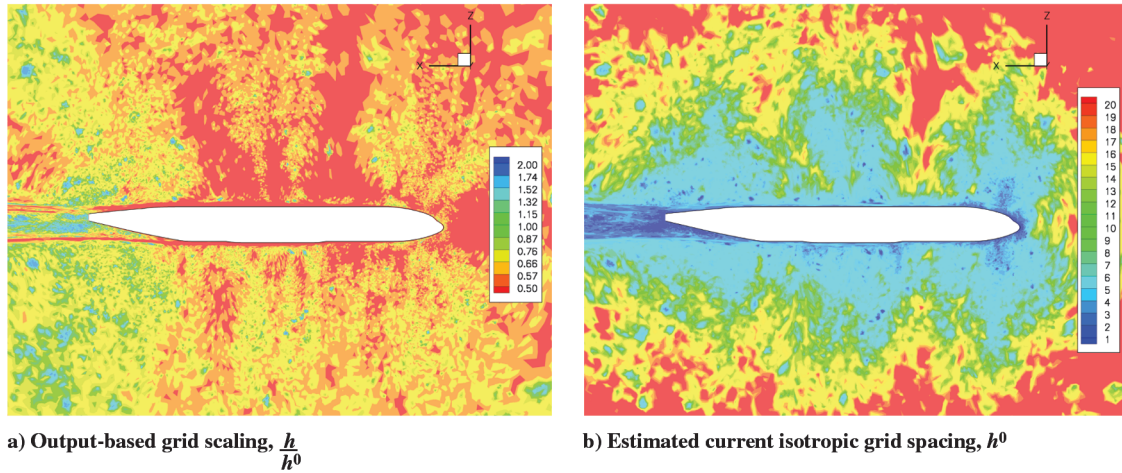


Fig. 12 Requested change and current isotropic spacing on the CRM symmetry plane for the penultimate adapted grid.

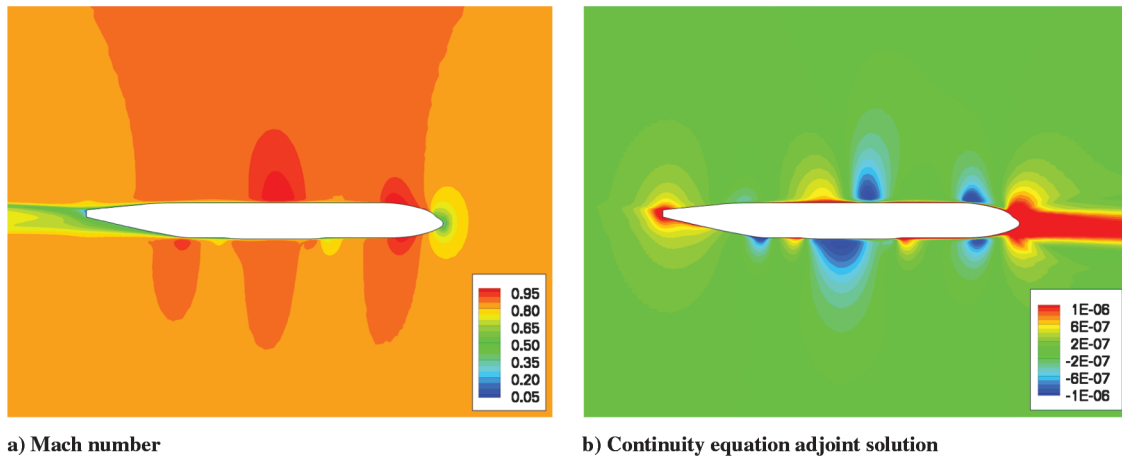


Fig. 13 Mach number and adjoint solution on the CRM symmetry plane.

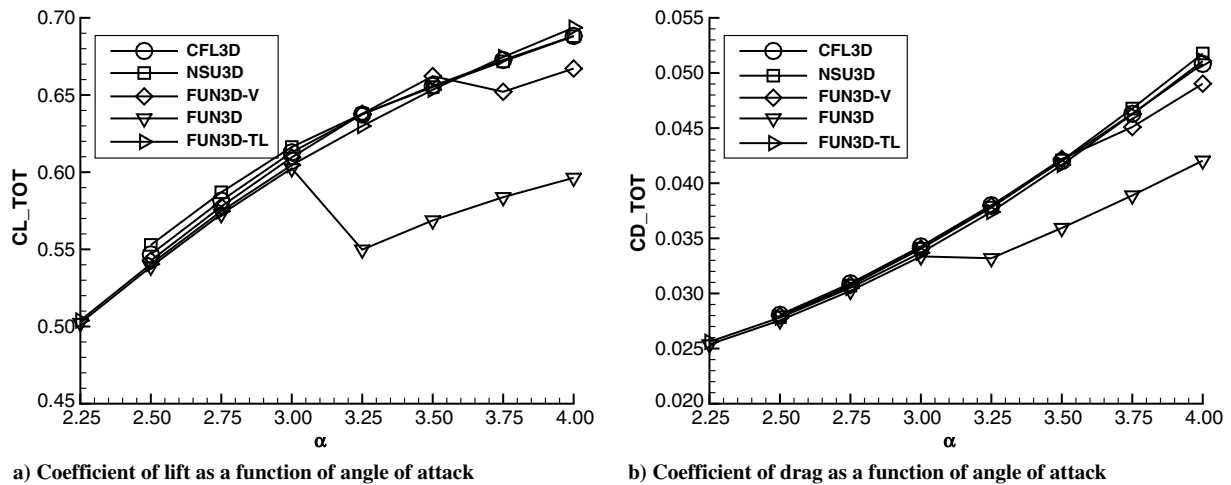


Fig. 14 Buffet study total forces for L3 grid.

pitching moment coefficient CM_{TOT} in Fig. 15, where the CM_{TOT} axis is reversed. CM_{TOT} trends changes abruptly at the same α as the abrupt CL_{TOT} change for FUN3D and FUN3D-V.

The abrupt reductions in forces are accompanied by a significant increase in wing-root separation bubble size (Fig. 16). Figure 16a is the butt line of the spanwise extent of the separation bubble BL_{BUB} as a function of α . The wing-root junction is at butt line 120.267, indicating the bubble is small at low α . Figure 16b is the fuselage station of the forward extent of the separation bubble FS_{BUB} . The

trailing edge of the wing-root junction is at the 1458.68 fuselage station, and the vertical axis has been reversed. A lower fuselage station implies a larger forward bubble extent.

FUN3D-TL has a very small bubble that remained the same size over the range of α examined. No bubble is reported for CFL3D or NSU3D. The FUN3D and FUN3D-V predicted that separation bubbles grow with increasing α . FUN3D shows a dramatic increase in lateral and forward extent at 3.25 deg α , and FUN3D-V shows a similar increase at 3.75 deg α . The α trends of the forces (Fig. 14) and

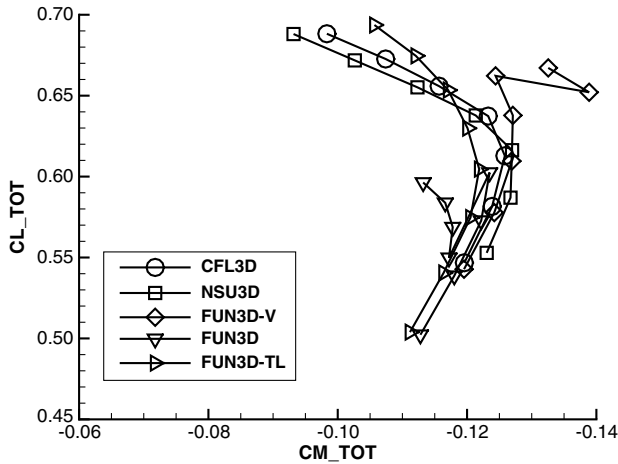


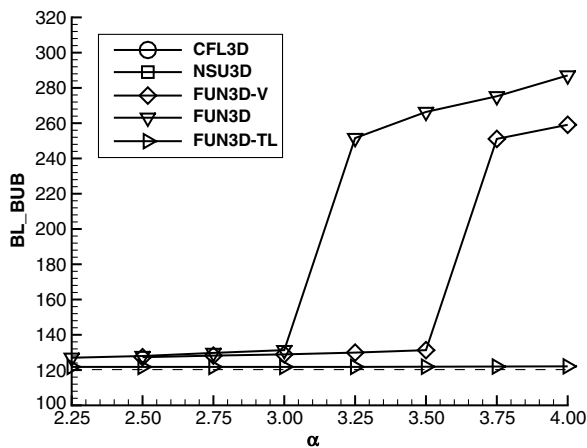
Fig. 15 Coefficient of lift as a function of pitching moment coefficient for L3 grid.

moment (Fig. 15) also change at the same α with rapid separation extent increases.

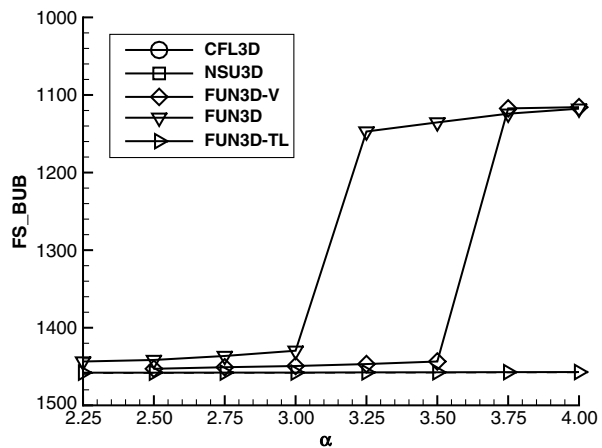
The value of the ϕ function of the Venkatakrishnan limiter is examined for FUN3D-V to illustrate potential differences between the reconstruction of FUN3D and FUN3D-V. Figure 17 shows the limiter function with constant butt line 151.074- and 697.333-volume slices near 13 and 60% spans. Figure 17a has two levels of nested

zoom to show details of the outer edge of the boundary layer and control volume adjacent to the solid wall. The upper wing shock, wake, outer boundary layer, and first control volume on the wall are areas where the Venkatakrishnan limiter is active (with a value of $\phi < 1.0$). Although the limiter function ϕ is close to one, in the majority of the field at an angle of attack of 3.25, it has a dramatic effect on the side-of-body separation (Fig. 16), forces (Fig. 14), and pitching moment (Fig. 15).

Coefficient of skin-friction color contours and coefficient of pressure contour lines in 0.1 increments are shown in Fig. 18. The series of subplots in Fig. 18 detail the separation bubble growth for FUN3D FNS with the unlimited scheme on the L3 hybrid grid. At $\alpha = 3.25$ and lower, a primary wing shock is seen on the upper surface of the wing in the coefficient of the pressure contour line cluster that parallels the wing trailing edge. The skin friction is low in the wing-root junction behind the intersection of the primary wing shock and the fuselage. The wing-root separation is contained in this low skin-friction region. The skin friction has also decreased behind the outer wing shock. At $\alpha = 3.50$ and above, the wing-root separation region has moved forward to the start of the adverse pressure gradient. The displacement of the streamlines due to the separation region has forced the primary wing shock to a forward location where the coefficients of pressure contour lines are clustered. The outer wing skin friction increases with the change in upper wing shock topology. The skin friction then continues to decrease behind the outer wing shock as angle of attack is increased. The upper wing shock locations (clusters of coefficient of pressure contour lines) appear to correlate with the initiation of wing-root separation.

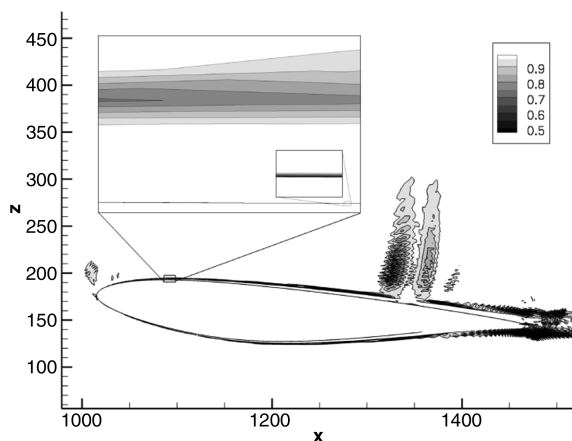


a) Lateral extent of the wing-root separation

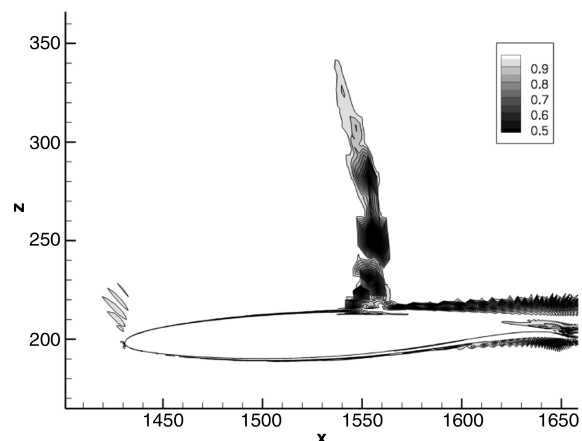


b) Longitudinal extent of the wing-root separation

Fig. 16 Wing-root separation bubble extent for the buffet study on the DPW committee grids. No separation reported for CFL3D or NSU3D.



a) $\eta = 0.1306$



b) $\eta = 0.6028$

Fig. 17 Value of the Venkatakrishnan limiter ϕ for the x -momentum equation at $\alpha = 3.25$.

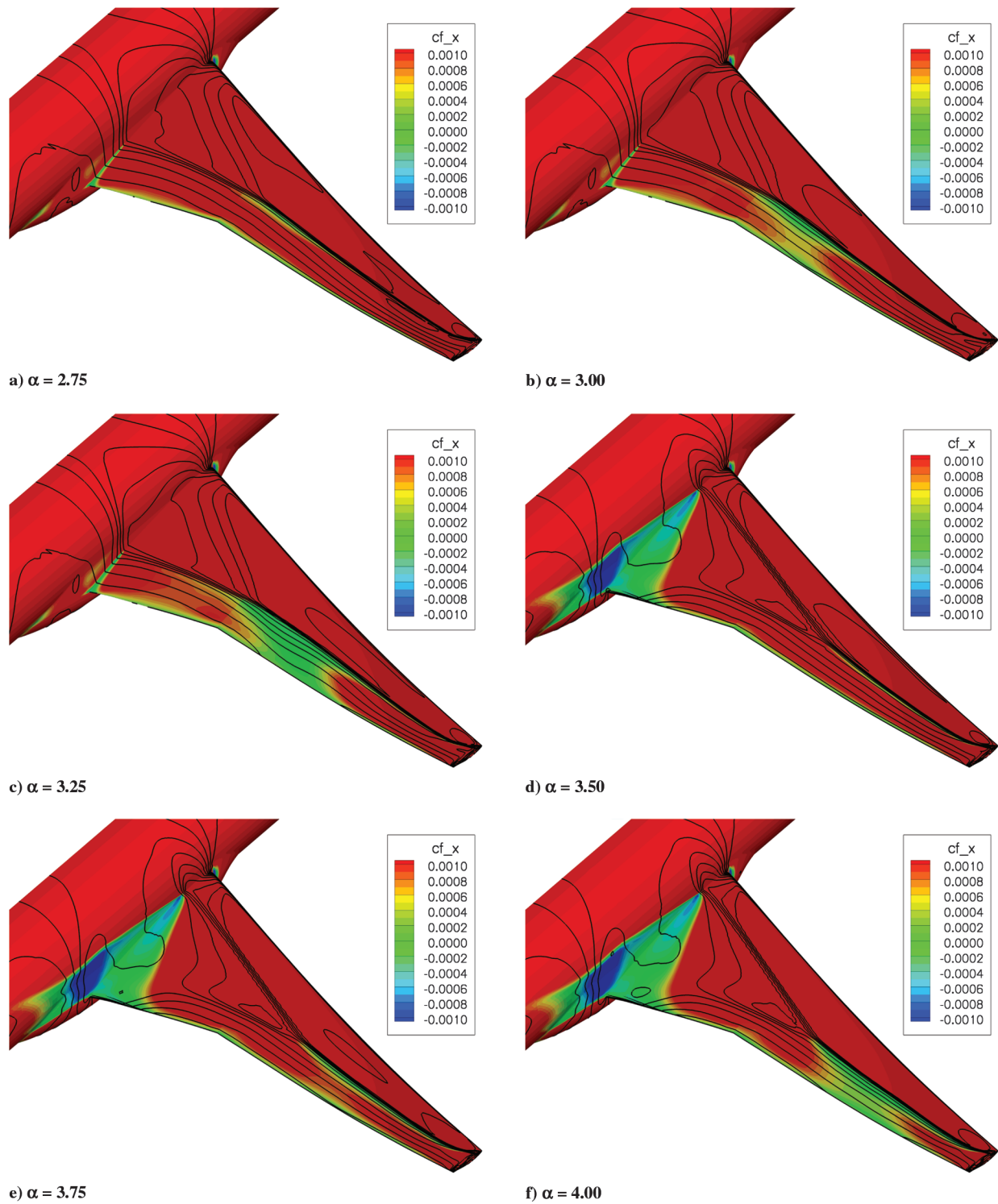


Fig. 18 X component of skin-friction color contours and coefficient of pressure contour lines for FUN3D FNS with the unlimited scheme on the L3 hybrid grid.

D. Buffet Study (Custom Grids)

In addition to the L3 DPW-V grid, grids based on a DPW-IV grid and custom grids are analyzed for the buffet study. These grids are designated DPW4T for the DPW-IV grid and CUSTT for the custom grid. Later in this paragraph the grid generation method is mentioned (VGRID). The FNS unlimited reconstruction FUN3D scheme is used on all of the grids in this section. This allows these different grid topologies to be evaluated with the same scheme. The number of nodes and elements in these custom grids are listed in Table 3. Both tetrahedral grids, DPW4T and CUSTT, are generated with VGRID [55]. The mixed-element grids, DPW4M and CUSTM, are created by merging the boundary-layer elements of DPW4T and CUSTT,

respectively [54]. A small number of Steiner nodes are required to complete the tetrahedra merging process [54], so the mixed-element grids have slightly more nodes than the original purely tetrahedral grids. The CUSTT and CUSTM custom grids have twice the total

Table 3 Other grids examined				
Grid	Nodes	Prisms	Pyramids	Tetrahedra
DPW4T	7,036,245	0	0	41,497,260
DPW4M	7,053,021	10,520,438	59,938	9,899,950
CUSTT	14,579,511	0	0	85,524,780
CUSTM	14,625,035	13,321,168	102,366	45,584,164

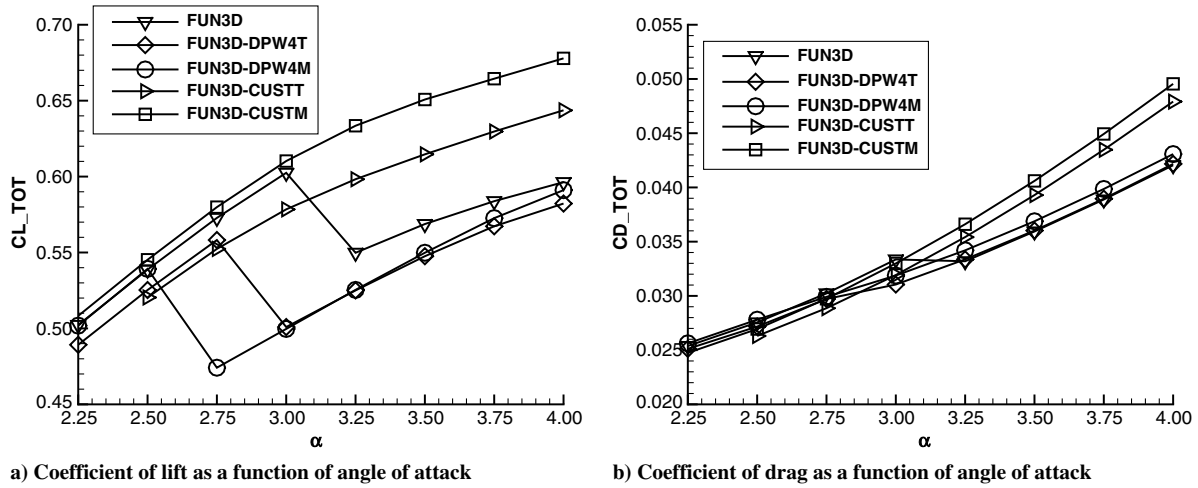


Fig. 19 Buffet study total forces for L3 and custom grids.

node count of the DPW4T and DPW4M grids and three times the total node count of the DPW-V L3 grid.

The DPW4T tetrahedral and DPW4M mixed-element grids are based on the mixed-element medium no-tail grid described by Lee-Rausch et al. [25], where the FUN3D calculations used FNS and the Venkatakrishnan limiter. The VGRID sources associated with the horizontal tail have been omitted to coarsen the grid in the tail region but retain the wing grid resolution of Lee-Rausch et al. [25].

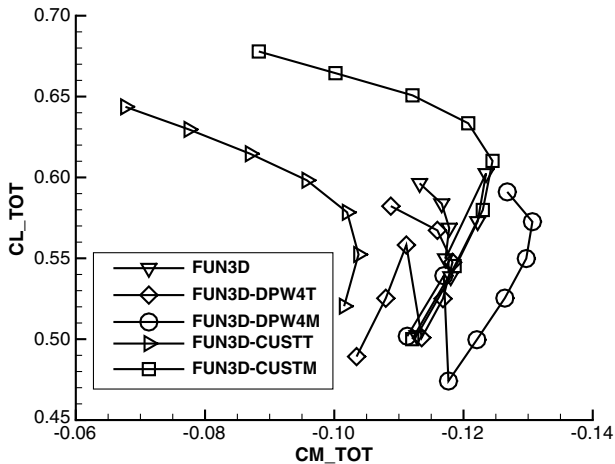


Fig. 20 Coefficient of lift as a function of pitching moment coefficient for L3 and custom grids.

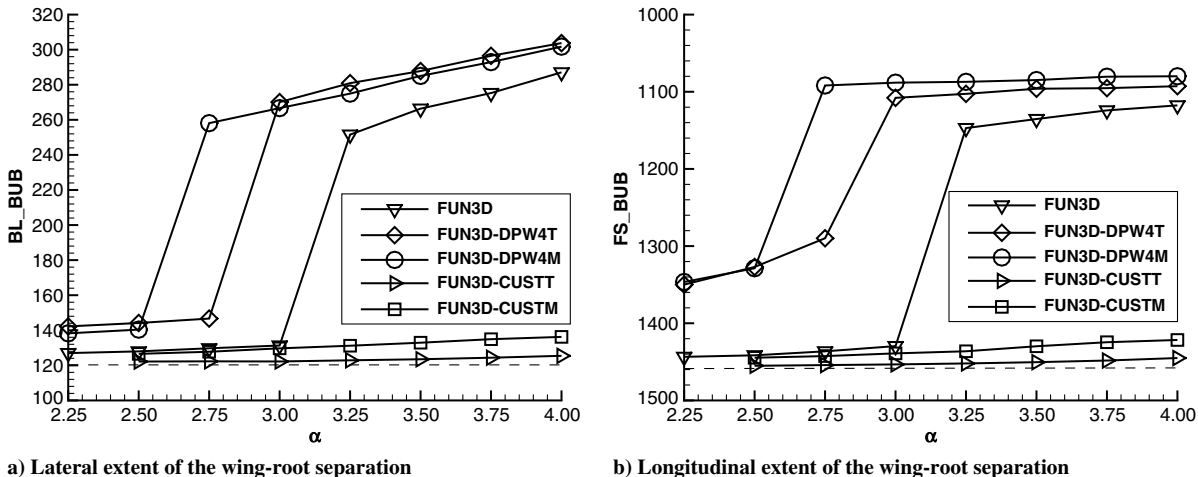
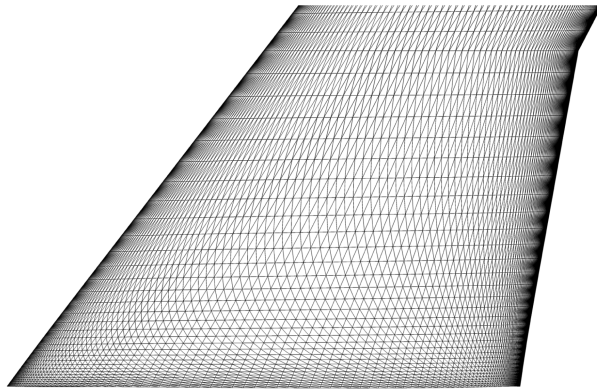


Fig. 21 Wing-root separation bubble extent for the buffet study for L3 and custom grids.

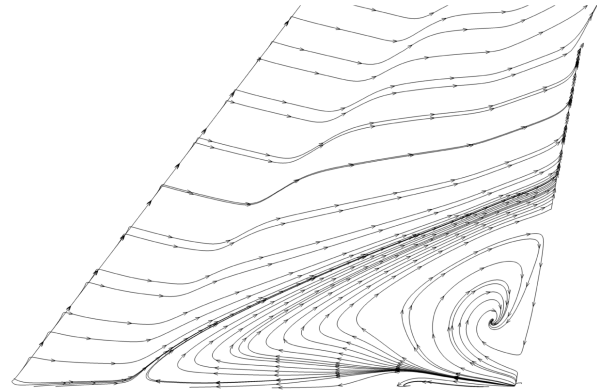
CUSTT has a measured $y^+ \ll 1$ and is created to be independent of the L3 mesh distribution. It uses VGRID advancing layer parameters of $rate1 = 0.15$, $rate2 = 0.02$, and $\delta1 = 0.0015$. CUSTT and L3 have a similar number of points across the trailing edge at the root. CUSTT has seven times the spanwise density at the trailing edge near the wing root. However, the ratio of spanwise mesh densities varies along the chord. The L3 spanwise mesh is four times finer at midchord, and the CUSTT mesh is twice as fine at the leading edge. The CUSTT grid has the least resolution in the wing-root junction, but it is larger overall with less spanwise stretching.

The buffet study was repeated with these custom grids. CL_{TOT} and CD_{TOT} are plotted as α is increased in 0.25 deg increments in Fig. 19. CL_{TOT} is plotted as a function of CM_{TOT} in Fig. 20. The CM_{TOT} axis is reversed. The unlimited reconstruction FNS FUN3D calculation on the L3 hybrid grid is included for comparison. The mixed-element FUN3D-CUSTM produced larger CL_{TOT} and CD_{TOT} and a more negative CM_{TOT} than the tetrahedral FUN3D-CUSTT for the entire α range examined. FUN3D-DPW4T shows a large decrease in lift at a 3 deg angle of attack. FUN3D-DPW4M shows a large decrease in lift at a 2.75 deg angle of attack.

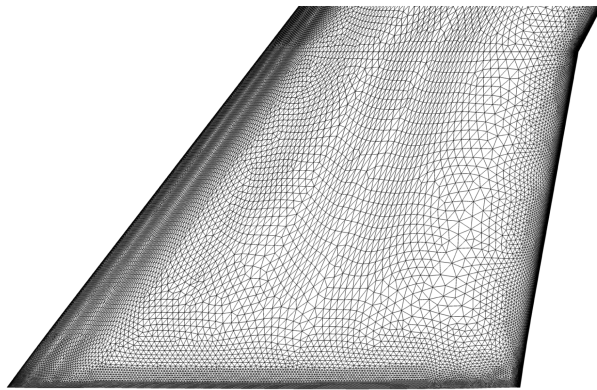
As with the workshop-provided grids, the abrupt reductions in forces are accompanied by a significant increase in wing-root separation bubble size (Fig. 21). Figure 21a is the butt line of the spanwise extent of the separation bubble BL_{BUB} as a function of α . The wing-root junction is at a butt line of 120.267, indicating the bubble is small at low α . Figure 21b is the fuselage station of the forward extent of the separation bubble FS_{BUB} . The trailing edge of the wing-root junction is at the 1458.68 fuselage station, and the



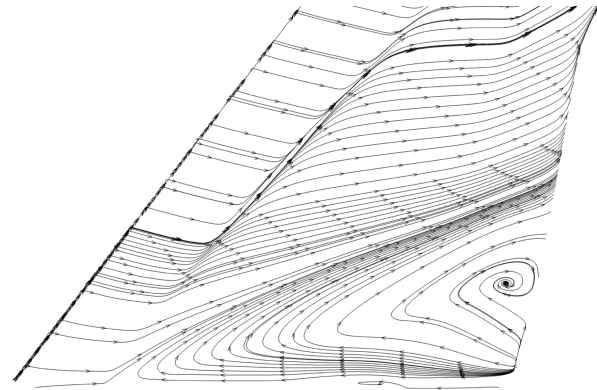
a) L3



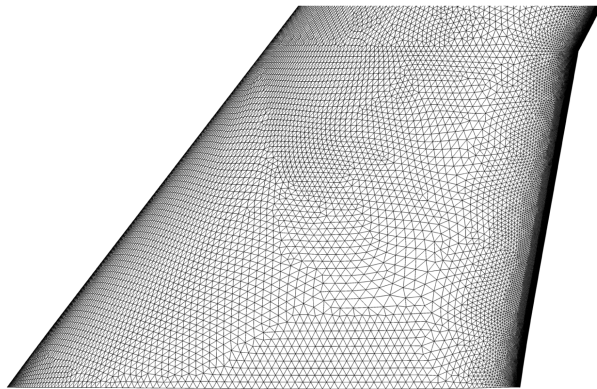
b) FUN3D



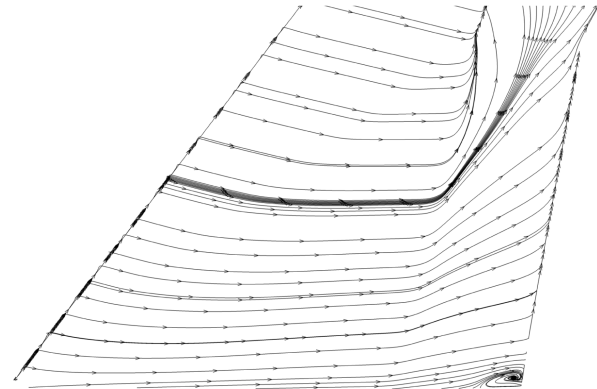
c) DPW4T and DPW4M



d) FUN3D-DPW4M



e) CUSTT and CUSTM



f) FUN3D-CUSTM

Fig. 22 Inboard section of the upper wing surface near the fuselage, surface grid, and streamlines at $\alpha = 4.00$.

vertical axis has been reversed. A lower fuselage station implies a larger forward bubble extent.

FUN3D-CUSTT has a very small bubble that remained the same size over the range of α examined. FUN3D-CUSTM also has a small bubble with a small increase in size with angle of attack. FUN3D, FUN3D-DPW4T, and FUN3D-DPW3M predicted separation bubbles that grow with increasing α . FUN3D-DPW4T and FUN3D-DPW4M have the largest separation bubble extents for the entire α range, which starts near the design condition of $CL_{TOT} = 0.5$. A dramatic increase in lateral and forward extent is shown by FUN3D at 3.25 deg α , FUN3D-DPW4T at 3.00 deg α , and FUN3D-DPW4M at 2.75 deg α . The α trends of the forces (Fig. 19) and moment (Fig. 20) also change at the same α with rapid separation extent increases.

The inboard portion of the upper wing is shown in Fig. 22. The surface grids and streamlines for the mixed-element grids at $\alpha = 4.00$

are shown for the unlimited reconstruction FNS FUN3D. The grid resolution is fine at the leading and trailing edges of all three grids. The DPW4T and DPW4M grids (Fig. 22c) have the finest wing-root grid (the lower portion of the subfigure). The L3 (Fig. 22a) grid has slightly less wing-root resolution. The CUSTT and CUSTM grids (Fig. 22e) have the coarsest wing-root grids. The grids with more wing-root grid resolution were also more likely to have wing-root separation at lower angles of attack in Fig. 21.

The large FUN3D and FUN3D-DPW3M separation bubbles traced by the streamline have similar structure and extent in Figs. 22b and 22d. The stronger shock locations can be observed initiating the abrupt outward turning of the streamlines. FUN3D-CUSTM has a small separation bubble isolated to the trailing edge near the fuselage in Fig. 22f. The strong primary wing shock parallel to the FUN3D-CUSTM trailing edge induces an abrupt outward turning of the streamlines, which is very clear near the trailing-edge Yehudi break.

VII. Buffet Study Wing-Root Separation Bubble

All the methods showed no separation bubble or a small bubble at the design condition of $CL = 0.5$. The large separation bubbles were observed in the higher angle-of-attack buffet study. The initiation of the separation region appears to be connected to the location of the primary upper wing shock. When the separation bubble grows dramatically, as angle of attack increases, it moves from the aft location of the primary wing shock to the start of the adverse pressure gradient in the wing root. Simultaneously, the primary wing shock moves forward due to the separation bubble displacement of upper wing streamlines. This shock and separation bubble interaction mechanism, as seen in this study and a review of DPW-IV and DPW-V publications, appears to be the dominate mechanism. The resultant shock, surface pressure, skin friction, and streamline topologies of the no/small separation bubble attractor and the large separation bubble attractor appear to be similar across a wide range of discretizations. However, it is less obvious how to know a priori if a particular discretization will exhibit the no, small, or large separation bubble topology.

CFL3D exhibited the no separation bubble topology with FNS. There is no reported separation bubble for NSU3D, which uses edge-based viscous terms that produce the TLNS approximation on orthogonal grids. FUN3D showed a wide range of separation bubble size for the various discretization options and grid topologies examined. On the DPW-V L3 grid, FUN3D with unlimited reconstruction and FNS showed a large increase in separation bubble size and drop in CL at $\alpha = 3.25$. FUN3D with the Venkatakrishnan limiter delayed the α with the large separation bubble size growth and reduced its lateral extent. The unlimited reconstruction and edge-based viscous operator producing a TLNS approximation resulted in the small separation bubble topology at $\alpha = 4.00$.

FUN3D with unlimited reconstruction and FNS was applied to grids with different grid topologies to examine the effect of wing-root grid refinement and separation bubble topology. A DPW-IV-based grid with finer wing-root grid resolution than the DPW-V L3 grid transitioned to the large separation bubble topology at a lower α than the L3 grid. This DPW-IV-based grid also had a larger bubble near the design condition of $CL = 0.5$. A custom grid with less wing-root grid resolution than the DPW-V L3 grid did not transition to the large separation bubble topology. The mixed-element versions of each of these grids had either transitioned at a lower α or had a larger bubble than the purely tetrahedral versions.

VIII. Conclusions

The CFL3D, FUN3D, and NSU3D computational methods were applied to the DPW-V CRM configuration. These included a structured grid method and two node-based mixed-element methods. The uniform grid refinement study at the design lift condition showed a tight grouping in drag for the finest grids. Drag-based adaptation was applied at the design lift condition. This included a combination of tetrahedral metric-based adaptation and mixed-element subdivision. The grid adapted drag results from a coarser grid approached those generated using a finer uniformly refined grid.

The buffet study using the committee-provided grids resulted in a larger range of forces and pitching moment coefficients than at the design condition. Abrupt reductions in lift and drag coefficients were correlated with an increase in side-of-body separation bubble size as angle of attack was increased. The initiation of the wing-root separation appears to be related to upper wing shock locations. Two distinct typologies emerged: a no/small separation bubble, and a large separation bubble.

It does not appear possible to anticipate, with absolute certainty, the separation bubble topology of a particular discretization based on its properties, but the following trends were observed. The use of edge-based viscous terms reduced the size of the bubble and resulted in higher lift and drag values without abrupt increases in side-of-body separation extent as compared to modeling FNS. This trend was also noted in the review of other published CRM results. However, the TLNS approximation changes modeling assumptions and may not be appropriate as a predictive tool.

The use of the Venkatakrishnan limiter on the committee-provided grids delayed the onset angle of attack of this effect as well as its severity. The participant-provided grids had a larger range of grid sizes and differences in force and moment coefficients. Converting a tetrahedral grid into a mixed-element grid increased the lift, drag, and separation bubble extent, which may be the result of a reduction in dissipation over the purely tetrahedral grids. Merging tetrahedra into mixed elements keeps approximately the same number of degrees of freedom for the node-based FUN3D because the existing node locations are maintained and only a fraction of a percent of new nodes are added during conversion. Grids with fine resolution of the wing-root juncture region showed more wing-root separation and were more likely to show abrupt increases in separation region extent.

In this study, the lowest dissipation scheme on the finest wing-root grid resolution produced the large separation bubble topology for FNS with the S-A turbulence model. Other published CRM results indicate that a large separation bubble is more likely on grids well resolved in the wing-root region. This indicates that the large separation bubble topology may be a valid solution to the RANS equations with the S-A turbulence model. However, this large separation bubble topology was not observed in wind-tunnel tests, indicating that there is still a need to improve modeling techniques to consistently predict the attached wing-root flow observed in the wind-tunnel test. Improved understanding may improve the reliability of predicting juncture flows in other situations.

Acknowledgments

James Thomas performed extensive exploratory work, improved the Jacobian-free Newton-Krylov method, implemented the negative Spalart-Allmaras (S-A) model, and developed the adaptive Courant-Friedrich-Levy scheme in FUN3D. Eric Nielsen extended the FUN3D adjoint solver to include a discretely consistent negative S-A model to enable the application of output-based adaptation for the Fifth Drag Prediction Workshop. Elizabeth Lee-Rausch and Christopher Rumsey shared experience gained on previous Drag Prediction Workshop studies. Dimitri Mavriplis provided the description of the NSU3D skin-friction calculation. The guidance of the anonymous reviewers was greatly appreciated.

References

- [1] Levy, D. W., Laflin, K. R., Tinoco, E. N., Vassberg, J. C., Mani, M., Rider, B., Rumsey, C. L., Wahls, R. A., Morrison, J. H., and Brodersen, O. P., et al., "Summary of Data from the Fifth AIAA CFD Drag Prediction Workshop," AIAA Paper 2013-0046, 2013.
- [2] Morrison, J. H., "Statistical Analysis of CFD Solutions from the Fifth AIAA Drag Prediction Workshop," AIAA Paper 2013-0047, 2013.
- [3] Morrison, J. H., Kleb, B., and Vassberg, J. C., "Observations on CFD Verification and Validation from the AIAA Drag Prediction Workshops," AIAA Paper 2014-0202, 2014.
- [4] Vassberg, J. C., DeHaan, M. A., Rivers, S. M., and Wahls, R. A., "Development of a Common Research Model for Applied CFD Validation Studies," AIAA Paper 2008-6919, 2008.
- [5] Vassberg, J. C., Tinoco, E. N., Mani, M., Rider, B., Zickuhr, T., Levy, D. W., Brodersen, O. P., Eisfeld, B., Crippa, S., and Wahls, R. A., et al., "Summary of the Fourth AIAA CFD Drag Prediction Workshop," AIAA Paper 2010-4547, 2010.
- [6] Morrison, J. H., "Statistical Analysis of CFD Solutions from the Fourth AIAA Drag Prediction Workshop," AIAA Paper 2010-4673, 2010.
- [7] Rivers, M. B., and Dittberner, A., "Experimental Investigation of the NASA Common Research Model," AIAA Paper 2010-4218, 2010.
- [8] Rivers, M. B., and Dittberner, A., "Experimental Investigations of the NASA Common Research Model in the NASA Langley National Transonic Facility and NASA Ames 11-Ft Transonic Wind Tunnel," AIAA Paper 2011-1126, 2011.
- [9] Bell, J. H., "Pressure-Sensitive Paint Measurements on the NASA Common Research Model in the NASA 11-Ft Transonic Wind Tunnel," AIAA Paper 2011-1128, 2011.
- [10] Zilliac, G. G., Pulliam, T. H., Rivers, M. B., Zerr, J., Delgado, M., Halcomb, N., and Lee, H., "A Comparison of the Measured and Computed Skin Friction Distribution on the Common Research Model," AIAA Paper 2011-1129, 2011.
- [11] Rivers, M. B., and Hunter, C. A., "Support System Effects on the NASA Common Research Model," AIAA Paper 2012-707, 2012.

- [12] Rivers, M. B., Hunter, C. A., and Campbell, R. L., "Further Investigation of the Support System Effects and Wing Twist on the NASA Common Research Model," AIAA Paper 2012-3209, 2012.
- [13] Hue, D., "CFD Investigations on the DPW-5 Configuration with Measured Experimental Wing Twist Using the elsA Solver and the Far-Field Approach," AIAA Paper 2013-2508, 2013.
- [14] Keye, S., Togiti, V., Eisefeld, B., Brodersen, O., and Rivers, M. B., "Investigation of Fluid-Structure-Coupling and Turbulence Model Effects on the DLR Results of the Fifth AIAA CFD Drag Prediction Workshop," AIAA Paper 2013-2509, 2013.
- [15] Sclafani, A. J., DeHaan, M. A., Vassberg, J. C., Rumsey, C. L., and Pulliam, T. H., "Drag Prediction for the NASA CRM Wing-Body-Tail Using CFL3D and OVERFLOW on an Overset Mesh," AIAA Paper 2010-4219, 2010.
- [16] Mani, M., Rider, B. J., Sclafani, A. J., Winkler, C., Vassberg, J. C., Dorgan, A. J., Cary, A., and Tinoco, E. N., "RANS Technology for Transonic Drag Prediction: A Boeing Perspective of the 4th Drag Prediction Workshop," AIAA Paper 2010-4221, 2010.
- [17] Yamamoto, K., Tanaka, K., and Murayama, M., "Comparison Study of Drag Prediction for the 4th CFD Drag Prediction Workshop using Structured and Unstructured Mesh Methods," AIAA Paper 2010-4222, 2010.
- [18] Spalart, P. R., "Strategies for Turbulence Modelling and Simulations," *International Journal of Heat and Fluid Flow*, Vol. 21, No. 3, 2000, pp. 252–263.
doi:10.1016/S0142-727X(00)00007-2
- [19] Yamamoto, K., Tanaka, K., and Murayama, M., "Effect of a Nonlinear Constitutive Relation for Turbulence Modeling on Predicting Flow Separation at Wing-Body Junction of Transonic Commercial Aircraft," AIAA Paper 2012-2895, 2012.
- [20] Spalart, P. R., and Allmaras, S. R., "A One-Equation Turbulence Model for Aerodynamic Flows," *La Recherche Aérospatiale*, Vol. 1, No. 1, 1994, pp. 5–21.
- [21] Hashimoto, A., Murakami, K., Aoyama, T., Yamamoto, K., Murayama, M., and Lahur, P. R., "Drag Prediction on NASA CRM Using Automatic Hexahedra Grid Generation Method," AIAA Paper 2010-1417, 2010.
- [22] Hashimoto, A., Ishiko, K., Lahur, P. R., Murakami, K., and Aoyama, T., "Validation of Fully Automatic Grid Generation Method on Aircraft Drag Prediction," AIAA Paper 2010-4669, 2010.
- [23] Brodersen, O., Crippa, S., Eisefeld, B., Keye, S., and Geisbauer, S., "DLR Results from the Fourth AIAA CFD Drag Prediction Workshop," AIAA Paper 2010-4223, 2010.
- [24] Crippa, S., "Improvement of Unstructured Computational Fluid Dynamics Simulations Through Novel Mesh Generation Methodologies," *Journal of Aircraft*, Vol. 48, No. 3, May–June 2010, pp. 1036–1044.
doi:10.2514/1.C031219
- [25] Lee-Rausch, E. M., Hammond, D. P., Nielsen, E., Pirzadeh, S. Z., and Rumsey, C. L., "Application of the FUN3D Unstructured-Grid Navier-Stokes Solver to the 4th AIAA Drag Prediction Workshop Cases," AIAA Paper 2010-4551, 2010.
- [26] Mavriplis, D. J., and Long, M., "NSU3D Results for the Fourth AIAA Drag Prediction Workshop," AIAA Paper 2010-4550, 2010.
- [27] Eliasson, P., and Peng, S.-H., "Influence of Turbulence Modelling and Grid Resolution in Computations of the DPW-4 CRM Configuration," AIAA Paper 2010-1416, 2010.
- [28] Eliasson, P., Peng, S.-H., and Tysell, L., "Computations from the 4th Drag Prediction Workshop Using the Edge Solver," AIAA Paper 2010-4548, 2010.
- [29] Vos, J. B., Sanchi, S., and Gehri, A., "DPW4 Results Using Different Grids Including Near-Field/Far-Field Drag Analysis," AIAA Paper 2010-4552, 2010.
- [30] Li, G., Li, F., Zhou, Z., and Sang, W., "Validation of a Multigrid-Based Navier-Stokes Solver for Transonic Flows," AIAA Paper 2010-4549, 2010.
- [31] Levy, D. W., and Chaffin, M. S., "Comparison of Viscous Grid Layer Growth Rate of Unstructured Grids on CFD Drag Prediction Workshop Results," AIAA Paper 2010-4671, 2010.
- [32] Hue, D., and Esquieu, S., "Computational Drag Prediction of the DPW4 Configuration Using the Far-Field Approach," *Journal of Aircraft*, Vol. 48, No. 5, 2011, pp. 1658–1670.
doi:10.2514/1.C031337
- [33] Vassberg, J. C., "A Unified Baseline Grid about the Common Research Model Wing-Body for the Fifth AIAA CFD Drag Prediction Workshop," AIAA Paper 2011-3508, 2011.
- [34] Sclafani, A. J., Vassberg, J. C., Winkler, C., Dorgan, A. J., Mani, M., Olsen, M. E., and Coder, J. G., "DPW-5 Analysis of the CRM in a Wing-Body Configuration Using Structured and Unstructured Meshes," AIAA Paper 2013-0048, 2013.
- [35] Nishikawa, H., Diskin, B., Thomas, J. L., and Hammond, D. P., "Recent Advances in Agglomerated Multigrid," AIAA Paper 2013-0863, 2013.
- [36] Murayama, M., Yamamoto, K., Hashimoto, A., Ishida, T., Uenoand, M., Tanaka, K., and Ito, Y., "Summary of JAXA Studies for the Fifth AIAA CFD Drag Prediction Workshop Using UPACS, S., and FaSTAR," AIAA Paper 2013-0049, 2013.
- [37] Gariépy, M., Malouin, B., Trépanier, J.-Y., and Laurendeau, E., "Far-Field Drag Decomposition Method Applied to the DPW-5 Test Case Results," AIAA Paper 2013-2507, 2013.
- [38] Illi, S. A., Fingskes, C., Lutz, T., and Krämer, E., "Transonic Tail Buffet Simulations for the Common Research Model," AIAA Paper 2013-2510, 2013.
- [39] Osusky, M., Boom, P. D., and Zingg, D. W., "Results from the Fifth AIAA Drag Prediction Workshop Obtained with a Parallel Newton-Krylov-Schur Flow Solver Discretized Using Summation-by-Parts Operators," AIAA Paper 2013-2511, 2013.
- [40] Ceze, M., and Fidkowski, K. J., "Drag Prediction Using Adaptive Discontinuous Finite Elements," AIAA Paper 2013-0051, 2013.
- [41] Scalabrin, L. C., and de Souza, R. F., "Grid Assessment Using the NASA Common Research Model (CRM) Wind Tunnel Data," AIAA Paper 2013-0052, 2013.
- [42] Krist, S. L., Biedron, R. T., and Rumsey, C. L., "CFL3D User's Manual (Version 5.0)," NASA Langley Research Center TM-208444, Hampton, VA, June 1998.
- [43] Roe, P. L., "Approximate Riemann Solvers, Parameter Vectors, and Difference Schemes," *Journal of Computational Physics*, Vol. 43, No. 2, 1981, pp. 357–372.
doi:10.1016/0021-9991(81)90128-5
- [44] Anderson, W. K., and Bonhaus, D. L., "An Implicit Upwind Algorithm for Computing Turbulent Flows on Unstructured Grids," *Computers and Fluids*, Vol. 23, No. 1, 1994, pp. 1–22.
doi:10.1016/0045-7930(94)90023-X
- [45] Nielsen, E. J., "Aerodynamic Design Sensitivities on an Unstructured Mesh Using the Navier-Stokes Equations and a Discrete Adjoint Formulation," Ph.D. Thesis, Virginia Polytechnic Inst. and State Univ., Blacksburg, VA, 1998.
- [46] Burg, C. O. E., Sheng, C., Newman, J. C. III, Brewer, W., Blades, E., and Marcum, D. L., "Verification and Validation of Forces Generated by an Unstructured Flow Solver," AIAA Paper 2003-3983, 2003.
- [47] Burg, C. O. E., "Higher Order Variable Extrapolation for Unstructured Finite Volume RANS Flow Solvers," AIAA Paper 2005-4999, 2005.
- [48] Venkatakrishnan, V., "Convergence to Steady State Solutions of the Euler Equations on Unstructured Grids with Limiters," *Journal of Computational Physics*, Vol. 118, No. 1, 1995, pp. 120–130.
doi:10.1006/jcph.1995.1084
- [49] Diskin, B., Thomas, J. L., Nielsen, E. J., Nishikawa, H., and White, J. A., "Comparison of Node-Centered and Cell-Centered Unstructured Finite-Volume Discretizations: Viscous Fluxes," *AIAA Journal*, Vol. 48, No. 7, 2010, pp. 1326–1338.
doi:10.2514/1.44940
- [50] Allmaras, S. R., Johnson, F. T., and Spalart, P. R., "Modifications and Clarifications for the Implementation of the Spalart-Allmaras Turbulence Model," *Seventh International Conference on Computational Fluid Dynamics (ICCFD7)*, ICCFD Paper ICCFD7-1902, 2012.
- [51] Eisenstat, S. C., Elman, H. C., and Schultz, M. H., "Variational Iterative Methods for Nonsymmetric Systems of Linear Equations," *SIAM Journal on Numerical Analysis*, Vol. 2, No. 2, April 1983, pp. 345–357.
doi:10.1137/0720023
- [52] Mavriplis, D. J., and Venkatakrishnan, V., "A Unified Multigrid Solver for the Navier-Stokes Equations on Mixed Element Meshes," *International Journal of Computational Fluid Dynamics*, Vol. 8, No. 4, 1997, pp. 247–263.
doi:10.1080/10618569708940807
- [53] Mavriplis, D. J., "Multigrid Strategies for Viscous Flow Solvers on Anisotropic Unstructured Meshes," *Journal of Computational Physics*, Vol. 145, No. 1, 1998, pp. 141–165.
doi:10.1006/jcph.1998.6036
- [54] Mavriplis, D. J., and Pirzadeh, S., "Large-Scale Parallel Unstructured Mesh Computations for Three-Dimensional High-Lift Analysis," *Journal of Aircraft*, Vol. 36, No. 6, 1999, pp. 987–998.
doi:10.2514/2.2540
- [55] Pirzadeh, S. Z., "Three-Dimensional Unstructured Viscous Grids by the Advancing-Layers Method," *AIAA Journal*, Vol. 34, No. 1, 1996, pp. 43–49.
doi:10.2514/3.13019

- [56] Park, M. A., and Carlson, J.-R., "Turbulent Output-Based Anisotropic Adaptation," AIAA Paper 2010-0168, 2010.
- [57] Park, M. A., Lee-Rausch, E. M., and Rumsey, C. L., "FUN3D and CFL3D Computations for the First High Lift Prediction Workshop," AIAA Paper 2011-0936, 2011.
- [58] Venditti, D. A., "Grid Adaptation for Functional Outputs of Compressible Flow Simulations," Ph.D. Thesis, Massachusetts Inst. of Technology, Cambridge, MA, 2002.
- [59] Park, M. A., "Anisotropic Output-Based Adaptation with Tetrahedral Cut Cells for Compressible Flows," Ph.D. Thesis, Massachusetts Inst. of Technology, Cambridge, MA, Sept. 2008.
- [60] Bibb, K. L., Gnoffo, P. A., Park, M. A., and Jones, W. T., "Parallel, Gradient-Based Anisotropic Mesh Adaptation for Re-Entry Vehicle Configurations," AIAA Paper 2006-3579, 2006.
- [61] Park, M. A., and Darmofal, D. L., "Parallel Anisotropic Tetrahedral Adaptation," AIAA Paper 2008-0917, 2008.
- [62] Lee, H. C., and Pulliam, T. H., "Effect of Using Near and Off-Body Grids with Grid Adaption to Simulate Airplane Geometries," AIAA Paper 2011-3985, 2011.
- [63] Mavriplis, D. J., "Adaptive Meshing Techniques for Viscous Flow Calculations on Mixed Element Unstructured Meshes," *International Journal for Numerical Methods in Fluids*, Vol. 34, No. 2, 2000, pp. 93–111.
doi:10.1002/(ISSN)1097-0363
- [64] Labbé, P., Dompierre, J., Vallet, M.-G., Guilault, F., and Trépanier, J.-Y., "A Universal Measure of the Conformity of a Mesh with Respect to an Anisotropic Metric Field," *International Journal for Numerical Methods in Engineering*, Vol. 61, No. 15, 2004, pp. 2675–2695.
doi:10.1002/(ISSN)1097-0207
- [65] Borouchaki, H., Hecht, F., and Frey, P. J., "Mesh Gradation Control," *International Journal for Numerical Methods in Engineering*, Vol. 43, No. 7, 1999, pp. 1143–1165.
- [66] Loseille, A., Dervieux, A., and Alauzet, F., "Fully Anisotropic Goal-Oriented Mesh Adaptation for 3D Steady Euler Equations," *Journal of Computational Physics*, Vol. 229, No. 8, 2010, pp. 2866–2897.
doi:10.1016/j.jcp.2009.12.021